DIGITAL LIBRARY

dspace.vutbr.cz

Micro- and Nanorobots Meet DNA

URSO, M.; PUMERA, M.

Advanced Materials for Optics and Electronics

vol. 32, iss. 37, pp. 1-19

ISSN (Online): 1616-3028

DOI: http://dx.doi.org/10.1002/adfm.202200711

Accepted manuscript

This is the peer reviewed version of the following article URSO, M.; PUMERA, M. Micro- and Nanorobots Meet DNA, Advanced Materials for Optics and Electronics, 2022, vol. 32, no. 37, p. 1-19. ISSN: 1616-3028, which has been published in final form at http://dx.doi.org/10.1002/adfm.202200711.

This article may be used for non-commercial purposes in accordance with Wiley Terms and Conditions for Use of Self-Archived Versions. This article may not be enhanced, enriched or otherwise transformed into a derivative work, without express permission from Wiley or by statutory rights under applicable legislation. Copyright notices must not be removed, obscured or modified. The article must be linked to Wiley's version of record on Wiley Online Library and any embedding, framing or otherwise making available the article or pages thereof by third parties from platforms, services and websites other than Wiley Online Library must be prohibited.

This is the peer reviewed version of the following article: Urso, M., & Pumera, M. (2022). Micro-and Nanorobots Meet DNA. Advanced Functional Materials, 2200711, which has been published in final form at https://doi.org/10.1002/adfm.202200711. This article may be used for non-commercial purposes in accordance with Wiley Terms and Conditions for Use of Self-Archived Versions. This article may not be enhanced, enriched or otherwise transformed into a derivative work, without express permission from Wiley or by statutory rights under applicable legislation. Copyright notices must not be removed, obscured or modified. The article must be linked to Wiley's version of record on Wiley Online Library and any embedding, framing or otherwise making available the article or pages thereof by third parties from platforms, services and websites other than Wiley Online Library must be prohibited.

Micro- and Nanorobots meet DNA

*Mario Urso and Martin Pumera**

Dr. M. Urso, Prof. M. Pumera
Future Energy and Innovation Lab, Central European Institute of Technology, Brno University of Technology, Purkyňova 656/123, 612 00 Brno, Czech Republic
E-mail: Martin.Pumera@ceitec.vutbr.cz

ORCID Mario Urso: 0000-0001-7993-8138
ORCID Martin Pumera: 0000-0001-5846-2951

Keywords: nanomotors, micromotors, DNA, RNA, aptamers, oligonucleotides, nucleic acids, motion-based sensing, fluorescence, gene delivery, gene silencing, water remediation

DNA, the well-known molecule that carries the genetic information of almost all forms of life, represents a pivotal element in formulating intelligent and versatile micro/nanorobotic systems. DNA-functionalized micro/nanorobots have opened new and exciting opportunities in many research areas due to the synergistic combination of self-propulsion at the micro/nanoscale and the high specificity and programmability of DNA interactions. Here, we critically reviewed their designs and applications, which span from the use of DNA as the fuel to chemotactically power nanorobots toward cancer cells to DNA as the main building block for sophisticated phototactic biorobots, DNA nanodevices to self-monitor microrobots' activity status, DNA and RNA sensing, nucleic acids isolation, gene therapy, and water purification. We also share our perspective on future directions of the field, envisioning DNA-mediated reconfigurable assemblies of nanorobotic swarms.

1. Introduction

DNA is the most famous biological molecule, carrying the genetic information for the development and functions of living beings through sequences of four nucleotides: adenine (A), thymine (B), cytosine (C), and guanine (G). Functional information encoded in DNA covers the sequence-determined binding of proteins, reactivity to enzymes, catalytic properties, and the recognition of low-molecular-weight substrates or macromolecules.[1] DNA mainly adopts the form of a double-stranded helix through A–T and G–C Watson–Crick base pairing. The helix has a diameter of 2 nm and a long persistence length of 50 nm, making DNA a quite stiff nanoscale polymer.[2] Watson–Crick base pairing is highly specific, reversible, tunable in strength, and programmable. Moreover, DNA is biodegradable and can be rapidly synthesized and modified using automated methods. Therefore, it represents the ideal building block for formulating sophisticated structures.[3]

On these bases, DNA nanotechnology was invented in the early 1980s, and it has exponentially grown since then.[4] Indeed, exclusively using DNA as an engineering material, from simple molecules to complex molecular machines that move or process information at the nanoscale, has been realized with customized sizes and shapes, controllable surface chemistry, and dynamic function.[5,6] Different research areas can be identified within this field, including sensing based on nucleic acids' recognition ability, drug delivery to living cells, DNA-mediated self-assembly of colloidal systems, and biocomputing.[7,8]

Micro/nanorobots are at the forefront of materials science and nanotechnology research due to the synergy between the unique and enhanced physicochemical properties of micro/nanoscale materials with the active motion dimension.[9–11] These smart small-scale robotic systems are designed in such a way to harvest energy from the surrounding environment and convert it into a powerful propulsive force, similar to bacteria.[12–14] Their autonomous movement improves their activity, overcoming the limits of passive diffusion and allowing them to reach previously inaccessible locations. At the same time, they are devised to perform intricate tasks, finding applications in sensors, medicine, and water purification.[15–21]

DNA and micro/nanorobots have come into contact in the last decade. Consequently, an increasing number of works has been reported, demonstrating how the marriage between these two technologies promises to revolutionize all research areas. This review presents the most advanced designs and applications of DNA-modified micro/nanorobots (**Figure 1**). It is

worth noting that the micro/nanorobots described here are nano- to microscale structures, moving at relatively high speeds, ranging from a few to hundreds of μm s^{-1}. These are distinct from DNA molecular machines such as the DNA walkers, which are molecular- to nanoscale structures moving up to tens of nm s^{-1} due to "legs" that hybridize and destroy complementary nucleic acids immobilized on a surface.[22] Thus, we recommend a recent and relevant review for those readers interested in DNA molecular machines.[23] Instead, in this work, we focus on the new concepts and prospects resulting from the intersection between DNA and micro/nanorobotics. First, the actuation mechanisms of DNA-modified micro/nanorobots are briefly introduced. Then, innovative DNA-based strategies to power and monitor their propulsion are illustrated. Next, the applications of DNA-modified micro/nanorobots are extensively and critically discussed, including DNA and RNA motion- and fluorescence-based sensing, nucleic acids isolation, gene therapy, and water remediation. Finally, a perspective on future directions of the field is shared, predicting the development of DNA-programmable reconfigurable self-assemblies of nanorobotic swarms as a new class of intelligent, cooperative nanorobots.

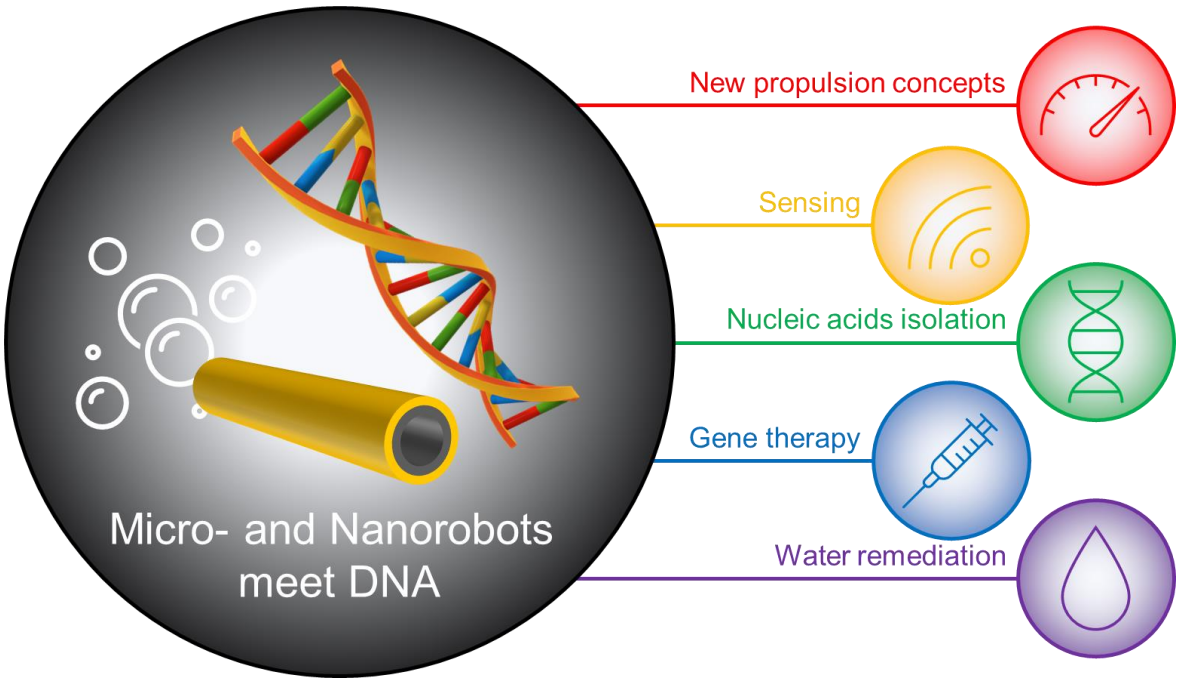

Figure 1. Research directions for DNA-modified micro/nanorobots presented in this review.

2. DNA-modified micro- and nanorobots actuation

Self-propulsion represents the principal requirement for a micro/nanorobot, allowing precise navigation toward the targeted site where desired tasks are performed or accelerating a catalytic or recognition process. This ability can be activated by external energy sources, such as light, acoustic, and magnetic fields, or local fuel consumption.[12] Each actuation mode has its *pros* and *cons.* Light-driven motion is primarily attractive for water remediation with photocatalytic semiconductors.[24–27] Enzymatic micro/nanorobots are more appropriate for biomedical applications but are limited to human body regions where a specific biomolecule is available.[28] Instead, magnetic manipulation offers high precision in the whole body without fuels.[29] In light of this, it is not surprising that preferential propulsion methods emerged while reviewing the literature on DNA-modified micro/nanorobots, including catalytic, acoustic, and magnetic. This section briefly introduces these motion mechanisms. We believe it can provide helpful information for readers unfamiliar with the field and facilitate the comprehension of the works presented in Sections 3 and 4.

Bubble-propelled tubular microrobots are the most reported among DNA-modified micro/nanorobots. For this reason, their fabrication procedure deserves to be shortly introduced. Their peculiar tubular structure is typically obtained by the membrane template-assisted deposition method, as illustrated in **Figure 2(a)**.[30,31] A commercially available membrane (for example, polycarbonate) serves as the template for depositing an outer functional layer (*e.g.*, Au or various polymers) followed by an inner Pt layer. The depositions are carried out by physical vapor deposition (PVD) processes (magnetron sputtering, electron-beam evaporation, atomic layer deposition) or electrochemical techniques requiring low-cost apparatus. However, metalization of the membrane, *i.e.*, the coating with a thin metal layer by PVD to improve its conductivity, is necessary for electrodeposition. The membrane's dissolution using an appropriate solvent (for instance, dichloromethane for polycarbonate) releases the microrobots. Figure 2(a) also reports the SEM images of a characteristic tubular microrobot showing the outer functional and inner Pt layers. The advantages of this approach are high simplicity, reproducibility, and monodispersity of the resulting microrobots. Alternatively, they can be prepared by the strain-assisted rolling of functional nanomembranes on polymers.[32] The propulsion of these rocket-like micromachines originates from the Pt-catalyzed decomposition of H_2O_2 fuel into H_2O and O_2 inside the tube. The nucleated O_2 bubbles are continuously ejected from the larger end of the tube, producing a strong propulsive force that pushes it forward, as displayed in Figure 2(a).[33] The presence

of low concentrations of surfactants, such as sodium dodecyl sulfate (SDS) and Triton-X, enhances bubble evolution, increasing microrobots' speed. The insertion of a ferromagnetic layer (Ni, Fe) between the outer and inner layers unlocks the possibility of magnetic steering and collectability.[28]

The membrane's pore size is a key parameter as it governs the dimension of the resultant machines. Therefore, nanoscale robots can be made by choosing a membrane with submicrometer pores. Moreover, tubular or rod/wire-like nanostructures can be achieved by filling the pores by tuning the parameters of the deposition technique. In this way, Au–Pt nanowires can be formed by the consecutive electrodeposition of Au and Pt segments inside nanopores, which propel in H_2O_2 solutions *via* self-electrophoresis as depicted in **Figure 2(b)**.[34] This mechanism is based on the generation of a gradient of charges, establishing a local electric field that drives the movement of a particle. For Au–Pt microrobots, oxidation of H_2O_2 occurs at the Pt side of the nanowire contemporarily to the reduction of H_2O_2 at the Au side. The excess of protons (H^+) at the Pt side produces an electric field pointing from Pt to Au. This, in turn, leads to the motion of the negatively charged nanorobots with the Pt side forward. It should be noted that the operation of these nanorobots is limited to low-ionic strength media, contrarily to the bubble-propelled tubular microrobots.[35] Again, this nanowire design can comprise magnetic features by introducing a ferromagnetic segment.

Enzymatic micro/nanorobots exploit enzyme-triggered chemical reactions to release the energy stored in the chemical bonds of a substrate (fuel) and translate it into active movement.[36] Catalase is the most used enzyme for the works presented in this review. Like Pt, it decomposes H_2O_2 at one of the highest enzymatic turnover rates (more than one million H_2O_2 molecules per catalase unit). This process leads to bubble-propulsion or self-phoresis.[37] Nevertheless, H_2O_2 toxicity may constitute a problem for biological applications. On the contrary, other enzymes functioning with biocompatible substrates, such as the urease–urea couple, are particularly attractive.[38] In this context, the following section presents the innovative concept of DNA-powered nanorobots. In general, the prerequisite for self-propulsion is to break the symmetry of the system, which can be attained by the asymmetric immobilization of the enzyme on the particle's surface as shown in **Figure 2(c)**.

Acoustically propelled nanorobots have been frequently employed for *in vivo* applications (**Figure 2(d)**).[39] Indeed, the use of ultrasound at sufficiently low amplitudes (MHz frequency range) does not harm biological samples, such as cells and tissues, while driving the movement of nanorobots. This actuation mode is based on the drifting caused by acoustic radiation forces (also called "acoustic radiation pressure") exerted on solid objects in a fluid

exposed to a sound wave field.[40] Simple ultrasound-powered nanorobots are represented by the Au nanowires fabricated by membrane template-assisted Au electrodeposition, whose surface can be facilely customized with thiolated DNA strands to exploit the strong Au–S covalent bond.

The excellent control over the movement of magnetic micro/nanorobots is particularly promising in biomedical applications.[29] Magnetic actuation requires incorporating a ferromagnetic element in the material's design. The motion is then based on the magneto-phoretic mechanism in magnetic field gradients, *i.e.*, spatially inhomogeneous fields, or the magnetic torque transfer under rotating magnetic fields.[41] The latter can be generated by systems of orthogonal coil pairs and are characterized by a rotating field vector. Helical structures are particularly attractive among the different magnetic micro/nanorobots. In fact, as depicted in **Figure 2(e)**, they efficiently traduce the rotational movement due to a low-strength rotating magnetic field into a translation movement in a screw-like manner.[40]

Table 1 reports the classification of the DNA-modified micro/nanorobots discussed in the following sections in terms of constituent materials, fabrication method, size, motion mechanism, DNA function, and application.

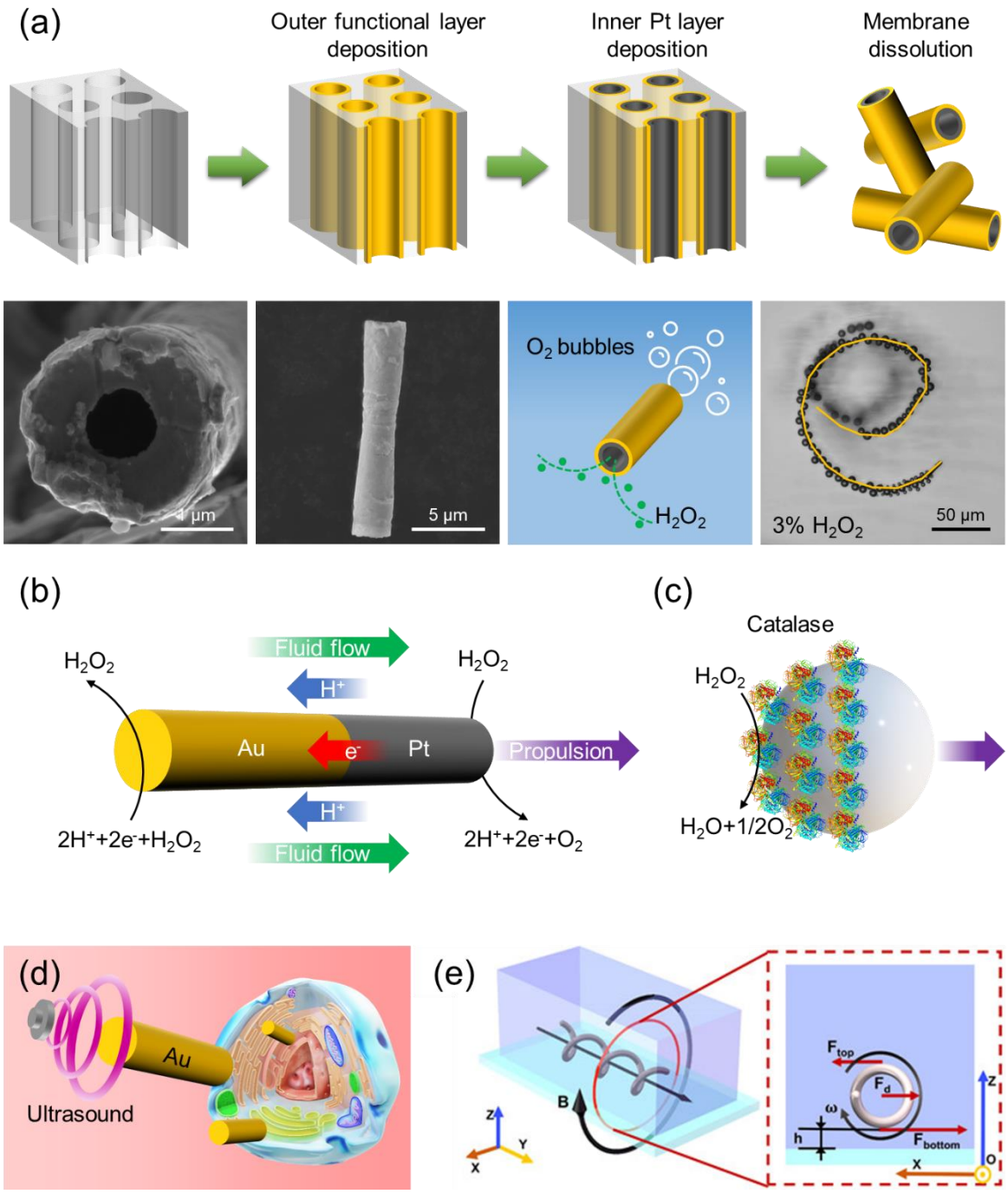

Figure 2. DNA-modified micro/nanorobots actuation modes. (a) Membrane template-assisted deposition method to fabricate bubble-propelled tubular microrobots. SEM images of tubular microrobots showing the outer functional and inner Pt layers. Propulsion mechanism of bubble-propelled tubular microrobots: the inner Pt layer catalyzes the decomposition of H_2O_2, producing O_2 bubbles; continuous ejection of O_2 bubbles pushes the microrobot forward. Time-lapse image showing the trajectory of a tubular microrobot in 3% H_2O_2 and 0.1% SDS after 1 s. Adapted with permission from [30]. Copyright 2021, Wiley. (b) Au–Pt nanowires' propulsion mechanism: H_2O_2 is oxidized at the Pt side and reduced at the Au side; the excess

of protons (H^+) at the Pt side produces an electric field pointing from Pt to Au, which induces the motion of the negatively charged nanorobots with the Pt side forward. (c) Catalase-modified Janus microrobots' propulsion mechanism by the catalyzed decomposition of H_2O_2. (d) Schematic illustration of ultrasound-powered Au nanowires for cell internalization. (e) Magnetic helical micro/nanorobots propulsion mechanism under a rotating magnetic field: the helix's rotation is traduced into a translational movement. Adapted with permission from [40]. Copyright 2020, AIP Publishing.

Table 1. Classification of DNA-modified micro/nanorobots.

Material	Fabrication	Size	Motion mechanism	DNA function	Application	Ref.
RhB-loaded DNase-functionalized PEG-Au-PAA/mSiO_2 nanoparticles	Chemical synthesis + DNase coupling + RhB loading	~170 nm	Catalytic DNA hydrolysis	Substrate	Targeting apoptotic tumor cells by chemotaxis	[42]
Peptide nanofiber forming unit-modified DNA microspheres	DNA hybridization	3-5 μm	Light-induced asymmetric growth of peptide nanofibers	Structural	n/a	[43]
Urease and DNA nanoswitch-functionalized hollow SiO_2 microparticles	Co-condensation method + functionalization with urease and DNA nanoswitches	~2 μm	Catalytic urea decomposition	Activity status indicator	n/a	[44]
FITC-labeled ssDNA-functionalized Au/Ni/Chitosan nanotubes	Membrane-assisted Ni electrodeposition + chitosan crosslinking + Au e-beam evaporation + DNA conjugation to Au	Diameter: 1.8 μm Length: 6 μm Thickness: 200 nm	External magnetic field	Traceability	Drug delivery	[45]
Segmented Au-Ni-Au-Pt nanowires	Sequential membrane-assisted electrodepositions	n/a	Catalytic H_2O_2 decomposition	Probe, target analyte	Motion-based DNA detection	[46]
ssDNA-modified PEDOT/Au microtubes	Membrane-assisted PEDOT and Au electrodepositions + DNA conjugation to Au	n/a	Bubble propulsion	Probe, target analyte	“Signal-on” motion-based DNA detection	[47]
Jellyfish-like Au/Ag/Ni/Au shells with a DNA probe sandwich and several catalase layers	Sequential sputtering depositions on sacrificial SiO_2 microspheres + cyclic alternate hybridization	20 μm	Bubble propulsion	Structural, probe, target analyte	Motion-based DNA detection	[48]
DNA-functionalized Pt NPs/Au NPs-PS beads	Pt and Au NPs chemical synthesis + DNA conjugation to Au NPs + loading on PS beads	6 μm	Catalytic H_2O_2 decomposition	Probe	Motion-based HIV-1 detection	[49]
FAM-labeled ssDNA-modified GO/Au nanowires	Membrane-assisted Au electrodeposition + incubation with GO and DNA	Diameter: ~300 nm Length: 4 μm	Acoustic field	Probe	Fluorescence recovery-based miRNA-21 detection	[50]
FAM-labeled ssDNA-modified erGO/Pt microtubes	Membrane-assisted erGO and Pt electrodepositions + incubation with DNA	Diameter: 3-4 μm Length: 4-13 μm Thickness: ~200 nm	Bubble propulsion	Probe, target analyte	Fluorescence recovery-based Reprimo detection	[51]

FAM-labeled ssDNA-modified MoS_2/Pt microtubes	Membrane-assisted MoS_2 and Pt electrodepositions + incubation with DNA	Diameter: 5 μm Length: ~10 μm Thickness: ~500 nm	Bubble propulsion	Probe	Fluorescence recovery-based miRNA-21 detection	[52]
TPE, FITC, aptamer, and catalase-modified PSMA/PSMA-HDA Janus fibers	Electrospinning of Janus fibers + cryocutting + catalase, aptamer, TPE, and FITC grafting	Length: 2-20 μm	Bubble propulsion	Probe	Ratiometric fluorescence detection of circulating tumor cells	[53]
ssDNA-modified Pt/PEDOT/W_5O_{14} microwires	W_5O_{14} by chemical vapor transport reaction + PEDOT by RF rotating plasma reactor + Pt sputtering + incubation with DNA	Length: ~10 μm	Bubble propulsion	Probe	Motion and fluorescence-based FAM-labeled miRNA-21 detection	[54]
FAM-labeled ssDNA-modified Au/PEDOT/Pt microtubes	Membrane-assisted Pt, PEDOT, and Au electrodepositions + incubation with DNA	Diameter: ~2 μm Length: ~12 μm	Bubble propulsion	Probe	Motion and fluorescence-based miRNA-21 detection	[55]
FAM-labeled ssDNA probe-modified Au/Pt microtubes	Membrane-assisted Au and Pt electrodepositions + incubation with DNA	Diameter: 1.5-2 μm Length: ~10 μm	Bubble propulsion	Probe	Acoustic waves-assisted motion and fluorescence-based miRNA-21 detection	[56]
FAM-labeled ssDNA-modified Au-Ni nanowires	Membrane-assisted Au and Ni electrodepositions + incubation with DNA	Diameter: 200 nm Length: 3 μm	Acoustic and/or magnetic field	Probe	Motion and fluorescence-based miRNA-21 detection and drug delivery	[57]
ssDNA-modified Au/Pt microtubes	Strain-assisted rolling of functional nanomembranes on polymers + Au sputtering + incubation with DNA	Diameter: ~2.5 μm Length: ~60 μm	Bubble propulsion	Probe	Extraction of nucleic acids from raw biological samples	[58]
Mixed binding aptamer-modified Au/Ni/Pt microtubes	Strain-assisted rolling of functional nanomembranes on polymers + Au and Ni sputtering + incubation with aptamers	Diameter: ~2.5 μm Length: ~60 μm	Bubble propulsion	Probe	Capture, transport, and release of thrombin	[59]
Aptamer-modified Au/Ni/MnO_2-PEI nanosheets	MnO_2 chemical synthesis + sonication with PEI + Ni and Au NPs electrodepositions + incubation with aptamers	n/a	Bubble propulsion	Probe	HL-60 cancer cells isolation and electrochemical detection	[60]
PEI-functionalized PPy-COOH/PPy/Ni/Pt microtubes	Sequential membrane-assisted electrodepositions + functionalization with PEI through carbodiimide chemistry	Diameter: 1-2 μm Length: ~10.5 μm Thickness: ~150 nm	Bubble propulsion	Target	Surface charge-controlled capture/transport/release of FITC-labeled nucleic acids	[61]
Lipoplexes-functionalized Ti/Ni/polymer micro helices	3D laser direct writing + Ni and Ti e-beam evaporation + incubation with lipoplexes	Diameter: ~5 μm Length: ~16 μm	Rotating magnetic field	Transfection	Targeted gene delivery to HEK-293 cells	[62]
GFP-labeled siRNA-loaded RCA DNA structure-modified Au nanowires	Membrane-assisted Au electrodeposition + rolling circle amplification	Diameter: ~300 nm Length: 4 μm	Acoustic field	Structural	Gene silencing by siRNA delivery to HEK-293 and MCF-7 cells	[63]

T-T mismatched DNA-functionalized Au/Pt microtubes	Membrane-assisted Au and Pt electrodepositions + functionalization with DNA	Diameter: 2.5-3 µm Length: ~10 µm	Bubble propulsion	Specific adsorption of Hg(II) by T-Hg(II)-T complex formation	Mercury-polluted waters remediation	[64]

3. DNA to power and monitor micro- and nanorobots propulsion

This section presents the strategies explored so far to induce the movement of micro/nanorobots through DNA. A unique example of nanorobots equipped with DNA nanodevices to self-monitor their motion status is also described.

Enzymatic micro/nanorobots are generally powered by hydrogen peroxide, glucose, and urea fuels at high concentrations (mM to M levels). Recently, biocompatible nanorobots fueled by ultra-low DNA concentrations (nM to μM levels) have been reported.[42] These nanorobots consisted of Janus nanoparticles asymmetrically functionalized with the enzyme DNase, which catalyzes DNA hydrolysis and chemotactically drives their propulsion toward DNA richer regions such as those close to apoptotic tumor cells (**Figure 3(a)**). Au-poly(acrylic acid) (Au-PAA) Janus nanoparticles were prepared *via* a multi-step, facile, and scalable synthetic procedure. Then, mesoporous silica ($mSiO_2$) was grown on the PAA side and loaded with rhodamine B (RhB) as a model drug. **Figure 3(b)** shows TEM images of the Au-PAA/$mSiO_2$ Janus nanoparticles (~170 nm in size). Next, the Au surface was passivated with methoxy-poly-(ethylene glycol)-thiol (mPEG-SH) to improve the nanorobots' stability. Finally, DNase was immobilized on the exposed PAA chains through the reaction between carboxylic groups of PAA and amino moieties of DNase.

RhB fluorescence allows the tracking of nanorobots. These displayed the typical Brownian motion in the absence of DNA and enhanced diffusion in its presence due to the DNase-induced DNA hydrolyzation. This reaction established an asymmetric product gradient leading to nanorobots movement *via* diffusiophoresis combined with a thermal effect due to heat generation. Nanorobots' speed increased with DNA concentration, from ~6 μm s^{-1} in 0 μM DNA to ~9 μm s^{-1} in 1.036 μM DNA. Their motion was isotropic as for Brownian particles in the absence of apoptotic tumor cells (**Figure 3(c)**). However, it turned into a directional motion toward apoptotic tumor cells due to the abnormal release of DNA in their surroundings (**Figure 3(d)**). This behavior, which occurs in nature for some organisms able to direct their movement according to environmental stimuli gradients, is called "chemotaxis." In this case, it was positive chemotaxis because the nanorobots moved toward the stimulus.

Moreover, the authors explored and demonstrated nanorobots' ability to seek tumor sites actively. Normal 3T3 cells and tumor 4T1 cells were placed into two reservoirs of a Y-shaped microfluidic channel (**Figure 3(e)**). Apoptosis of 4T1 cells was induced before injecting nanorobots into the third reservoir. By monitoring the fluorescence intensity in the three reservoirs, it was shown that nanorobots preferentially accumulate in the 4T1 cells reservoir

(**Figure 3(f)**). A control experiment using Janus nanoparticles without DNase indicated the uniform distribution of the nanoparticles in the two reservoirs with the cells. These findings prove the potential of such a new class of DNA-powered nanorobots to target, approach, and release drugs in the diseased site, which is highly demanded for tumor diagnosis and therapy. However, due to the lack of *in vivo* experiments, the applicability of these nanorobots in real scenarios and the enhanced therapeutic efficiency compared to conventional cancer treatments are not fully demonstrated. Additionally, nanorobots' recovery has not been considered.

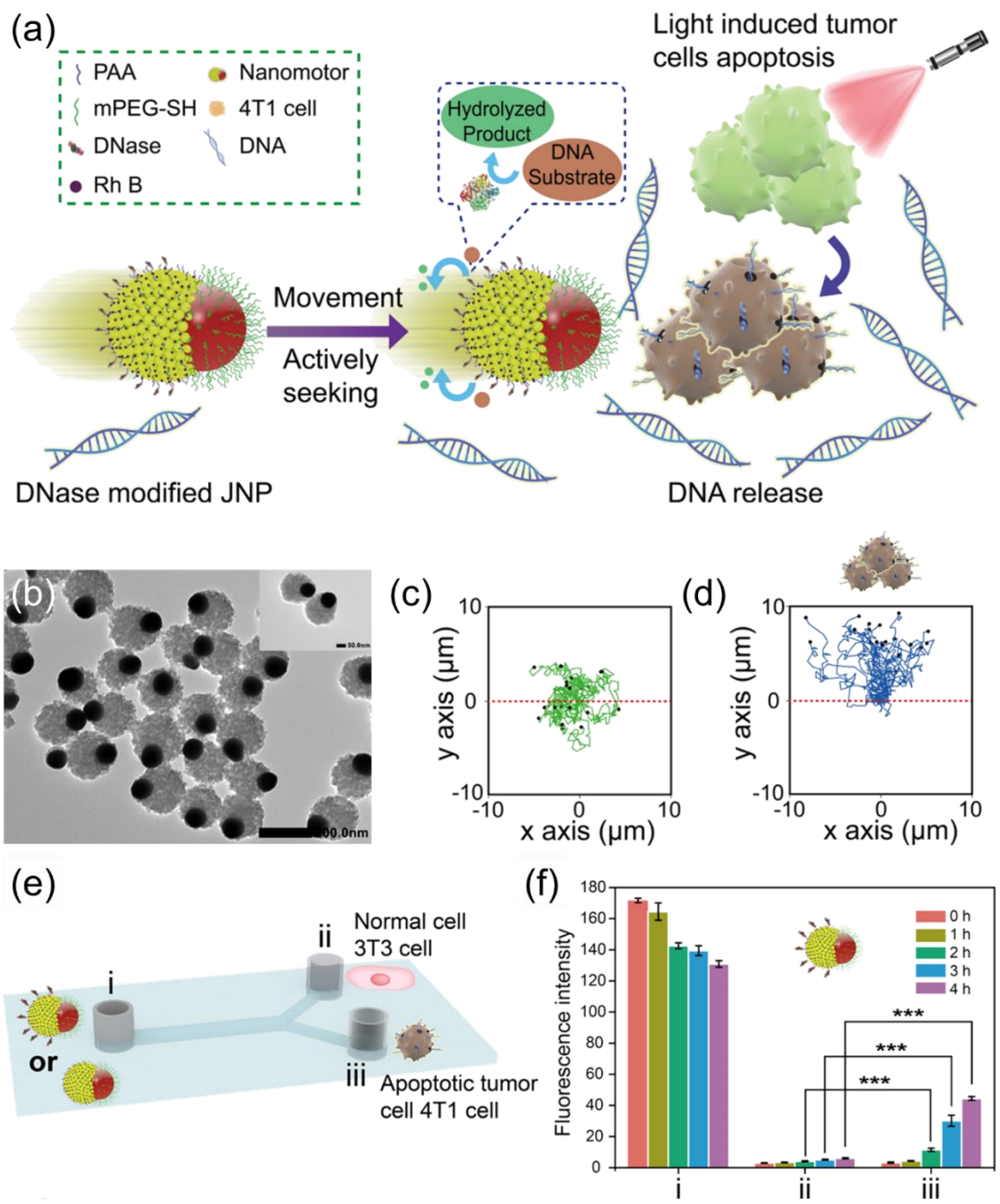

Figure 3. DNA-powered chemotactic nanorobots. (a) Schematic illustration of the motion mechanism of DNase-modified RhB-loaded PEG-Au-PAA/mSiO_2 Janus nanorobots by catalyzed DNA hydrolyzation and chemotaxis toward the DNA-rich region around apoptotic tumor cells. (b) TEM images of Au-PAA/mSiO_2 Janus nanoparticles. The scale bar is 200 nm (50 nm for the inset). (c) Trajectories of 20 nanorobots exhibiting isotropic motion in the absence of apoptotic tumor cells and (d) directional motion toward apoptotic tumor cells. (e) Chemotaxis experiment in a Y-shaped microchannel with nanorobots placed in reservoir i, normal 3T3 cells in reservoir ii, and apoptotic tumor 4T1 cells in reservoir iii. (f)

Fluorescence intensity in the three reservoirs as a function of time, indicating the progressive and preferential accumulation of nanorobots in the reservoir with apoptotic tumor 4T1 cells. Adapted with permission from [42]. Copyright 2021, American Chemical Society.

DNA can be used not only as a fuel but also as the main component to build light-driven micro/nanorobots.[43] This innovative concept is based on the asymmetric growth of peptide nanofibers on nucleospheres under UV-light irradiation. Nucleospheres are submicrometer- to micrometer-sized self-assembled DNA spheres obtained through the thermal annealing of three different single-stranded DNA (ssDNA) sequences with self-complementary sticky ends. These DNA microparticles possess the advantage of easy modification with functional molecules, which is crucial for the proposed propulsion strategy. By using a biotinylated ssDNA, biotin-containing nucleospheres were synthesized and modified with streptavidin and biotin-dT_{20} ssDNA (**Figure 4(a)**). Next, a peptide-DNA conjugate, made of FKFEFKFE nanofiber-forming unit and dA_{20} ssDNA linked by a photocleavable amino acid, was immobilized on the nucleospheres using the biotin-streptavidin interaction and DNA hybridization (**Figure 4(b)**). Confocal laser scanning microscopy (CLSM) images of nucleospheres exposed to UV-light irradiation for 3 min (**Figure 4(c)**) showed how the release of the peptide unit on the irradiated side of the nucleosphere resulted in the asymmetric formation of peptide nanofibers.

In the dark, these microrobots exhibited the characteristic isotropic trajectories of Brownian particles (**Figure 4(d)**). Under UV-light irradiation, they manifested a directional motion against the light source (**Figure 4(e)**), called "negative phototaxis." This behavior was due to the force generation caused by peptide nanofibers growth and the Marangoni effect owing to the surface tension gradient between the two sides of the microrobots. The speed was higher in the presence of an excess amount of peptide–DNA conjugate in solution, which assisted peptide nanofiber progression, reaching a value of ~5 μm min^{-1}. Furthermore, the propulsion persisted after turning off the UV-light source. This peculiar design serves as the inspiration for bio-microrobots mimicking natural phototactic systems. Nevertheless, the microrobots' speed is significantly lower than the aforementioned DNA-fueled nanorobots. In addition, despite the application of these microrobots has not been envisioned, the UV-light irradiation represents a major limitation, especially in biomedicine.

In another example of DNA-based microrobots where DNA has a structural/propulsive function, the DNA tile-tube assembly technique has been used to fabricate long artificial flagella. Once attached to iron oxide microspheres, these flagella transformed them into

bacteria-sized magnetic microrobots, enabling their movement under a rotating magnetic field by means of a flagellar bundle.[65]

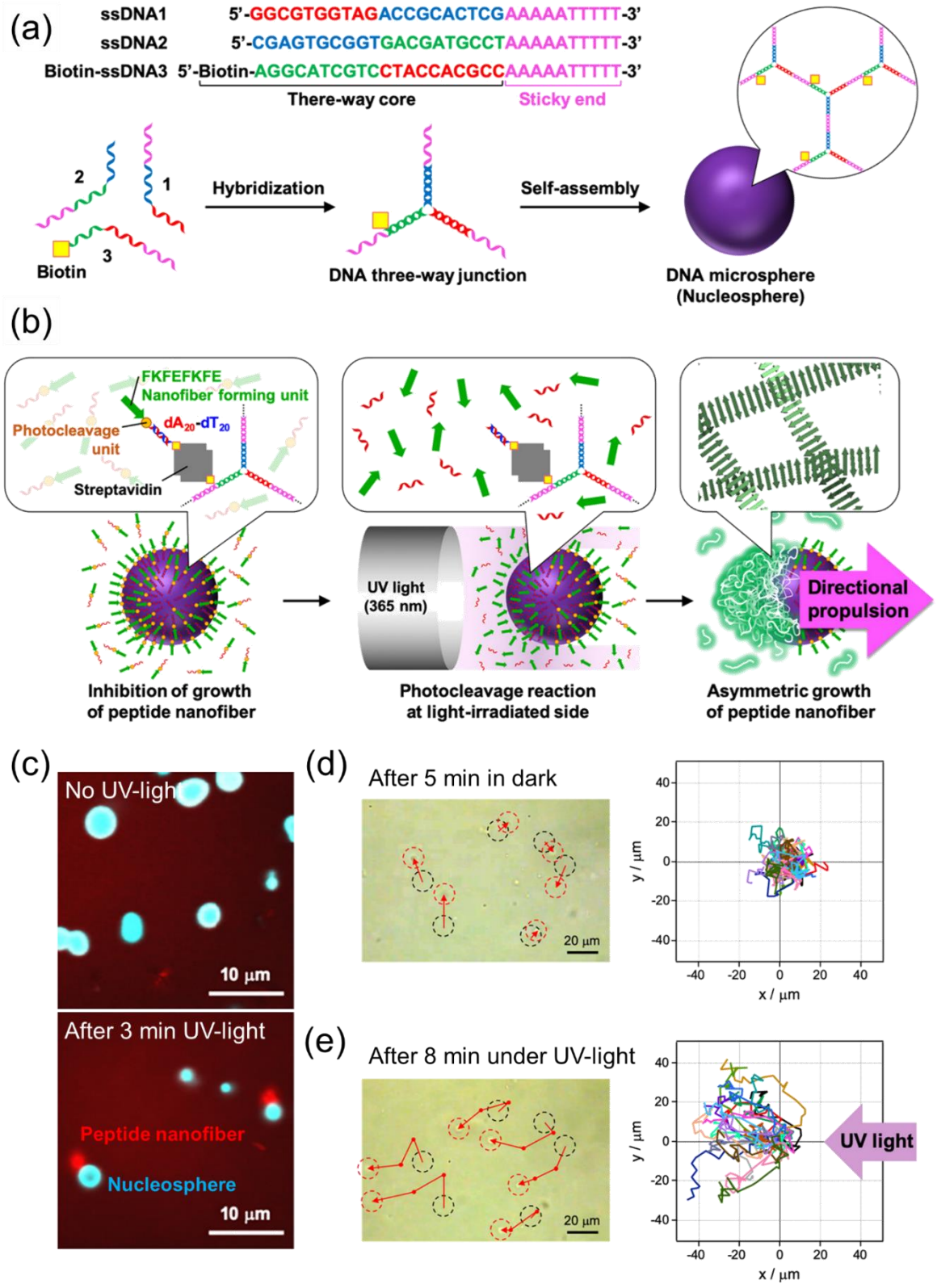

Figure 4. Light-driven phototactic DNA microrobots. (a) Schematic illustration of nucleospheres' preparation and (b) phototaxis due to the UV-light-induced asymmetric

growth of peptide nanofibers. (c) CLSM images of nucleosphere before and after 3 min under UV-light irradiation. Nucleospheres were stained with DAPI (cyan), and the nanofiber-forming unit was labeled with TMR (red). (c) Time-lapse images and trajectories of 20 microrobots showing isotropic Brownian motion after 5 min in the dark and (d) directional motion against the light source (negative phototaxis) after 8 min under UV-light irradiation. Adapted with permission from [43]. Copyright 2021, American Chemical Society.

DNA nanodevices responding to various biological and chemical stimuli hold great promise for the intelligentization of micro/nanorobots. In this regard, it has been demonstrated that pH-sensitive DNA nanoswitches allow real-time monitoring of microrobots' activity status (for instance, speed).[44] **Figure 5(a)** illustrates the fabrication of urea-powered microrobots. Briefly, a SiO_2 layer was grown on polystyrene (PS) beads using APTES and TEOS precursors. The PS core was removed by DMF, leaving hollow SiO_2 microcapsules with a size of ~2 μm (**Figure 5(b)**). These were functionalized with urease and DNA nanoswitches. Urease was included to induce microrobots motion *via* the catalyzed decomposition of urea into ammonia (NH_3) and carbon dioxide (CO_2) (**Figure 5(c)**). The nanoswitch, depicted in **Figure 5(d)**, consisted of a triplex DNA structure that could be opened or closed depending on the surrounding pH owing to pH-insensitive Watson–Crick interactions and pH-sensitive Hoogsteen interactions. Cyanine-3 (Cy3) fluorophore was conjugated to the duplex DNA, while cyanine-5 (Cy5) fluorophore was conjugated to the triplex-forming DNA strand to visualize the open/close grade of the nanoswitch. At acidic pH values (pH < 6), the nanoswitch was closed, and the proximity between Cy3 and Cy5 resulted in Förster Resonance Energy Transfer (FRET) emission. At higher pH values (pH > 6), the nanoswitch opened, and FRET emission was hindered. At the same time, a stronger Cy3 emission was detected, diminishing the FRET/Cy3 ratio.

This system permitted the visualization of the microrobots' status. In fact, by introducing 100 mM urea, microrobots were initially propelled at a speed of ~6 μm s^{-1} due to urea decomposition by urease. A FRET/Cy3 ratio of ~2 was registered in this stage. Contemporarily, the produced ammonia gradually increased the local pH around the microrobots, closing the nanoswitches and reducing FRET emission. Figure 5(e) shows the FRET/Cy3 ratio over time. The same trend was observed for the microrobots' speed (**Figure 5(f)**). This behavior was due to the decreasing urease activity (**Figure 5(g)**), which, in turn, lowered microrobots' speed and FRET/Cy3 ratio. Such correlation represents a smart approach for microrobots' speed imaging during their operation. Besides, it may be applied for evaluating intracellular and intra-tissue pH values. Still, microrobots' lifetime has to be

improved for practical applications since their speed decreased to less than 0.5 μm s^{-1} within 10 min.

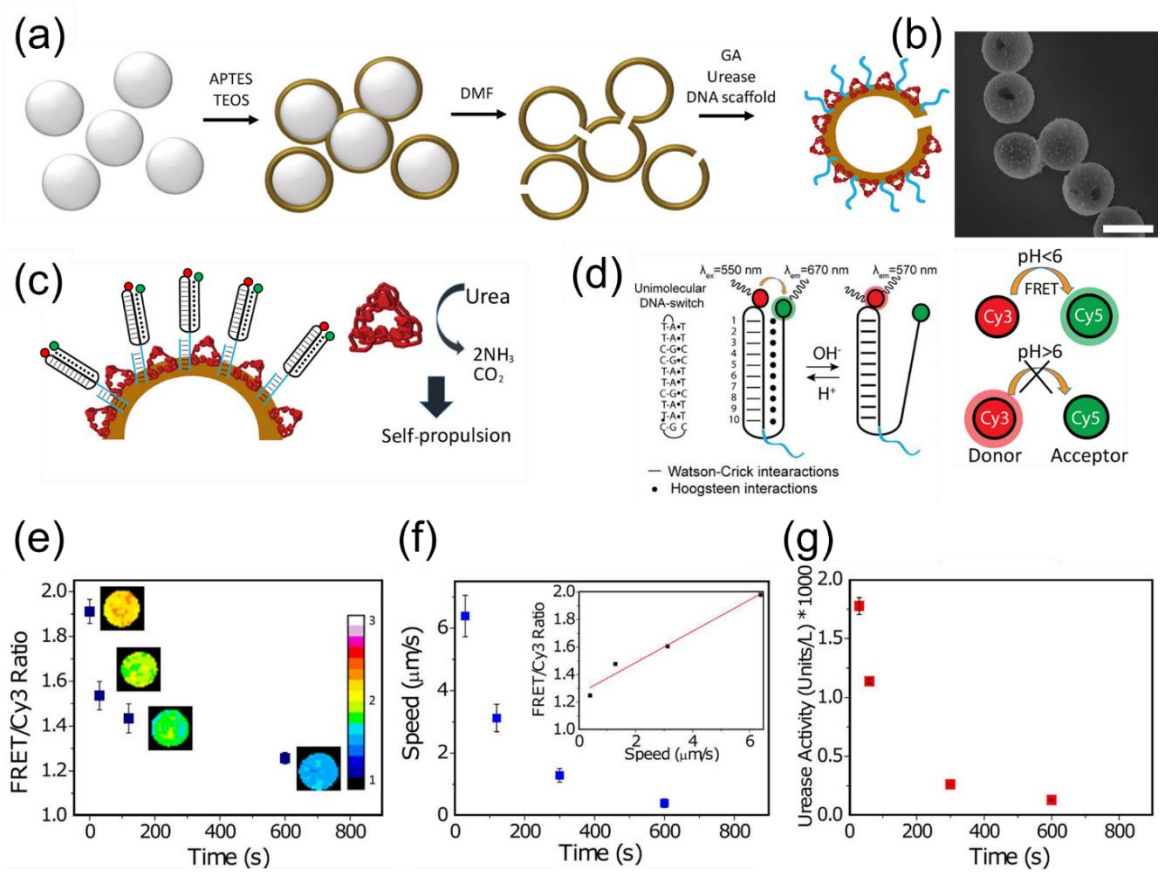

Figure 5. Self-sensing enzyme-powered DNA microrobots. (a) Schematic illustration of microrobots' fabrication. (b) SEM image of hollow SiO_2 microcapsules. The scale bar is 2 μm. (c) Schematic diagram of microrobots' propulsion mechanism and (d) DNA nanoswitches' operation at acidic and basic pH values. (e) FRET/Cy3 ratio of microrobots incubated with 100 mM urea at different times. CLSM images of a microrobot allowing the FRET/Cy3 ratio visualization. (f) Microrobots' speed at different times. The inset shows the correlation between speed and FRET/Cy3 ratio. (g) Microrobots' enzymatic activity at different times. Adapted with permission from [44]. Copyright 2019, American Chemical Society.

Tracing and monitoring the micro/nanorobots' position inside the human body is fundamental for biomedical applications. Fluorescence imaging represents a practical solution. Fluorescent isothiocyanate (FITC)-labeled DNA sequences can be used to introduce fluorescence to micro/nanorobots. For example, Ni nanotubes prepared by membrane

template-assisted electrodeposition were filled with a pH-responsive chitosan hydrogel for drug delivery. At the same time, their outer surface was coated by a gold layer to bind a FITC-labeled thiolated DNA sequence *via* Au–S bond. The resulting nanorobots were precisely manipulated using an external magnetic field and traced through the FITC fluorescence signal, enabling the selective release of drugs in the acidic environment of extracellular tumors.[45]

4. Applications of DNA-modified micro- and nanorobots

This section describes the most relevant contributions of DNA-modified micro/nanorobots in various application fields, ranging from DNA and RNA detection to the isolation of nucleic acids, gene therapy, and water purification.

4.1. DNA and RNA sensing by micro- and nanorobots

Traditional methods for DNA and RNA detection, including the highly sensitive and selective polymerase chain reaction (PCR), are expensive, time-consuming, and require laboratory instruments operated by trained personnel due to their complex operational protocols.[66] By contrast, the rapid diffusion of coronavirus disease 2019 (COVID-19) has demonstrated how crucial the timely identification and management of infectious diseases are. Recently, DNA-modified micro/nanorobots have opened new opportunities in this context. Different approaches can be identified according to the sensing mechanism: (1) motion-based sensors translate probe-target hybridization events into appreciable differences in micro/nanorobots' motion or speed; (2) fluorescent recovery-based sensors exploit micro/nanorobots' active movement to accelerate the hybridization, producing a detectable optical signal; (3) motion- and fluorescence-based sensors where both microrobots' fluorescence intensity and speed vary as a result of the hybridization. The most significant examples related to these three categories are presented below.

4.1.1. Motion-based sensing

Wang's research group introduced the concept of motion-based sensing for the first time.[67] This consists of using an optical microscope to track changes in micro/nanorobots' speed due to the presence of a target analyte. After proving that trace levels of Ag^+ ions enhanced the

speed of catalytic Au–Pt nanowires in H_2O_2, they extended the methodology for the transduction of DNA hybridization.[46] The sensor's operation principle is schematically illustrated in **Figure 6(a)**. A gold electrode functionalized with a thiolated ssDNA probe was used to capture Ag nanoparticles-tagged ssDNA target, forming a dsDNA. Upon exposure to H_2O_2, Ag nanoparticles quickly dissolved, releasing Ag^+ ions. The Ag^+ ions-rich H_2O_2 solution was employed to power fresh Au–Ni–Au–Pt nanowires prepared by membrane template-assisted electrodeposition, which moved *via* the self-electrophoretic mechanism represented in Figure 2(b). By incorporating a ferromagnetic Ni segment, linear trajectories were obtained under a magnetic field, allowing a straightforward comparison between tracks length at a fixed time interval for different amounts of DNA target. As expected, the nanorobots' track length in 10% H_2O_2 increased with DNA target concentration. A limit of detection (LoD) of 40 amol and 7 x 10^3 CFU μL^{-1} was measured for synthetic DNA target and 16S rRNA, released from *E. coli* pathogenic bacteria. The sensor exhibited high specificity against a variety of interferents and a reproducible response.

Later on, Nguyen and Minteer presented the "signal on" motion-based DNA sensing.[47] **Figure 6(b)** illustrates the working principle of the sensor. The inner Au layer of poly(3,4-ethylenedioxythiophene)/Au (PEDOT/Au) tubular microrobots, fabricated by membrane template-assisted electrodeposition, and Pt nanoparticles were modified with two ssDNA sequences, which were partially complementary to an ssDNA target. Without the target, microrobots' self-propulsion in H_2O_2 was not observed. Instead, it linked the Pt nanoparticles to the microrobots' inner layer when present. Hence, microrobots' bubble-propulsion in H_2O_2 was activated, likewise tubular microrobots with a compact Pt layer (Figure 2(a)). A non-complementary sequence did not trigger their motion, suggesting excellent selectivity. However, this sensor lacked sensitivity since the speed values for the 1 and 20 pmol DNA targets were relatively similar (157 and 222 $\mu m\ s^{-1}$ in 5% H_2O_2, respectively). Of note, compared to the previously described electrocatalytic nanowires, bubble-propelled microrobots allow operation in high-ionic strength solutions.

Wu and coworkers reported a different motion-based sensing approach, inducing a decrease in microrobots' speed rather than an increase.[48,68,69] For this purpose, the authors prepared jellyfish-like Au/Ag/Ni/Au shells (20 μm in size) by successive sputtering deposition of metals on sacrificial SiO_2 microspheres (**Figure 6(c)**). Before SiO_2 etching, the outer Au surface was blocked with 6-mercapto-1-hexanol (MCH). In this way, after SiO_2 etching, the shell's concave surface was modified with a DNA probe sandwich ("sensing unit") and several catalase layers ("power unit") by cyclic alternate hybridization assembly.

By doing so, the shells displayed bubble-propulsion even in low H_2O_2 concentrations (~25 μm s^{-1} in 0.25% H_2O_2). Then, the DNA detection was based on the release of the power unit due to the hybridization between the sensing unit and DNA target, causing the diminution of microrobot speed. An LoD of 10 nM was obtained with this method.

The proof-of-concept studies discussed above require an optical microscope operated by a specialized staff to record and measure micro/nanorobots' motion and speed after interacting with different DNA/RNA concentrations. As a result, the application of motion-based sensors could seem restricted to laboratories. On the other hand, a reliable, affordable, and compact motion-based sensor for HIV-1 infection has also been presented.[49] This integrated loop-mediated isothermal amplification (LAMP) reaction, DNA-modified catalytic microrobots, and cellphone-based optical sensing to record and track microrobot motion (**Figure 6(d)**). In particular, microrobots were made by asymmetrically coating polystyrene beads (6 μm in size) with Pt nanoparticles (4 nm) and ssDNA probe-modified Au nanoparticles (150 nm). Upon amplification of HIV-1 RNA by LAMP reaction, the microrobots captured the resulting amplicons. As a consequence, a large DNA tail was formed, obstructing microrobots' movement in H_2O_2 and, thus, decreasing their speed. This stratagem enabled the detection of HIV-1 at concentrations lower than the clinically relevant threshold of 1,000 virus particles mL^{-1} and the discrimination between positive and negative patients. The excellent sensitivity, selectivity, stability, rapidity (< 1 h), and low cost (< $5) of the proposed sensor promise timely management of other infectious diseases in the future. Furthermore, the proposed cellphone-based sensing system could be extended to the other motion-based detection strategies and enable their concrete application.

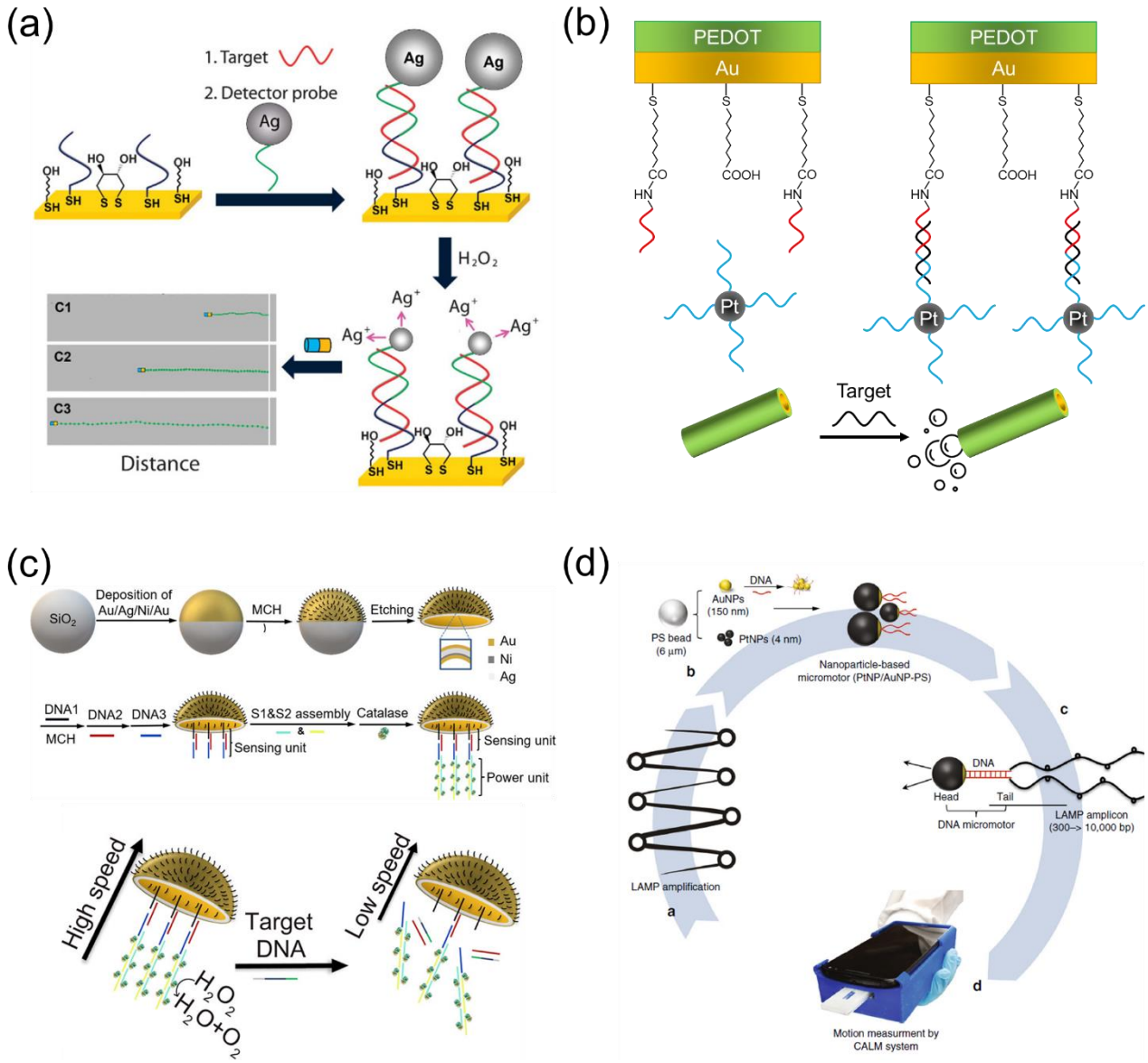

Figure 6. Motion-based DNA sensing strategies. (a) A DNA-modified Au electrode captures an Ag nanoparticles-tagged DNA target. Ag nanoparticles dissolution in H_2O_2 causes the release of Ag^+ ions. This solution is used to fuel electrocatalytic Au-Ni-Au-Pt nanorobots along linear trajectories under magnetic alignment. Straight-line distance signals for increasing DNA target concentrations (C1 < C2 < C3) are visualized by optical microscopy. Adapted with permission from [46]. Copyright 2010, Springer Nature. (b) The inner surface of PEDOT/Au tubular microrobots and Pt nanoparticles are functionalized with non-complementary DNA sequences. The latter are partially complementary to a DNA target. By connecting the Pt nanoparticles to microrobots, the target triggers their bubble-propulsion in H_2O_2, leading to the "signal on" motion-based DNA sensing. (c) Jellyfish-like Au/Ag/Ni/Au shells, comprising a DNA probe sandwich ("sensing unit") and several catalase layers ("power unit") prepared by cyclic alternate hybridization DNA assembly, detect a target DNA

via the hybridization-induced release of the power unit, which causes a decrease of microrobots' bubble-propulsion speed in H_2O_2. Adapted with permission from [48]. Copyright 2019, American Chemical Society. (d) HIV-1 motion-based detection using a cellphone system: LAMP reaction amplifies the HIV-1 RNA; DNA-modified catalytic microrobots, consisting of polystyrene microbeads coated by Pt and DNA-modified Au nanoparticles, capture the resulting amplicons; the formed DNA tail decelerates the microrobots' catalytic propulsion in H_2O_2; a cellphone system measures variations of the microrobots' speed, which allows it to sense HIV-1 at the clinically relevant threshold of 1,000 virus particles mL^{-1}. Reproduced with permission from [49]. Copyright 2018, Springer Nature.

4.1.2. Fluorescence recovery-based sensing

Various micro/nanorobots, differing in the material's design or actuation mechanism, have demonstrated the fluorescence detection of cancer biomarkers in a rapid, sensitive, and specific manner. Among the targeted cancer biomarkers is microRNA 21 (miRNA-21), a small RNA highly overexpressed in solid tumors, such as those of the brain, head and neck, esophagus, breast, lung, stomach, pancreas, colon, and prostate.[70] Consequently, several works have been focused on miRNA-21 sensing.

First, Wang et al. reported acoustically powered nanorobots for real-time detection of miRNA-21 in single cells.[50] Au nanowires (~300 nm in diameter, 4 μm in length) were fabricated by membrane template-assisted electrodeposition and further modified with a self-assembled monolayer (SAM) of cysteamine to immobilize graphene oxide (GO) sheets covalently. Then, the nanorobots' surface was functionalized with a fluorescein amidine (FAM)-labeled ssDNA probe. **Figure 7(a)** shows the miRNA-21 detection strategy based on: (i) the FRET quenching of the dye's fluorescence signal caused by the π–π interaction between GO and FAM-labeled ssDNA, and (ii) fluorescence recovery as a result of the release and hybridization of the FAM-labeled ssDNA with the miRNA-21 target. The intracellular detection of endogenous miRNA-21 was investigated using the breast cancer cell line MCF-7. The nanorobots showed fast internalization and effective movement inside the cells under the application of ultrasound (6 V, 2.66 MHz), which accelerated the hybridization process leading to a quick "OFF-ON" switching of the fluorescence in single MCF-7 cells within 5 min of incubation. The method's selectivity was confirmed by a control experiment with HeLa cells, which are characterized by a lower expression of miRNA-21 compared to MCF-7. Indeed, the fluorescence intensity of MCF-7 was 44 times higher than HeLa cells after the treatment with nanorobots.

Subsequently, the same nanorobots were employed to detect human papillomavirus (HPV)-associated head and neck cancer and breast cancer. In the first case, the FAM-labeled ssDNA probe was complementary to the HPV16 E6 mRNA target. After 15 min incubation under ultrasound, nanorobots allowed the successful discrimination between HPV-negative and HPV-positive human oropharyngeal cancer (OPC) cells *via* the fluorescence-recovery mechanism.[71] In the second case, nanorobots were modified with a FAM-labeled DNA aptamer, which allowed the detection of the overexpressed amplified in breast cancer 1 (AIB1) protein in MCF-7 cells.[72]

Bubble-propelled tubular microrobots have been used for the "OFF-ON" fluorescence detection of Reprimo (RPRM), a gastric cancer biomarker.[51] These microrobots were prepared by membrane template-assisted deposition through the electrochemical reduction of GO (erGO), followed by the electrodeposition of a Pt layer and the modification with a FAM-labeled RPRM probe. Microrobots propulsion in a solution of 1.5% H_2O_2 and 5 μM RPRM target produced a strong fluorescence signal within 2 min, six times higher than the one registered for static microrobots. It is worth mentioning that similar aptamer-modified erGO/Pt tubular microrobots have also been applied to detect different toxins through the same mechanism.[73,74]

The 2D layered material molybdenum disulfide (MoS_2) can replace the role of GO in the fluorescence recovery-based detection of miRNA-21 and proteins.[52] Tubular microrobots were created by membrane template-assisted electrodeposition of MoS_2 and Pt. Microrobots exhibited a high speed of 370 μm s^{-1} in 1% H_2O_2, which was attributed to the granular morphology of the Pt layer. Analogously to GO, MoS_2 quenched the FAM-labeled ssDNA probe's fluorescence, enabling the "OFF-ON" fluorescence detection of miRNA-21 within 5 min in 1% H_2O_2. The same microrobot was used to sense thrombin through a fluorescein isothiocyanate (FITC)-labeled DNA aptamer probe.

Li and coworkers presented the capture-induced ratiometric fluorescence detection of circulating tumor cells (CTCs) by self-motile microrobots (**Figure 7(b)**).[53] Despite not being strictly related to DNA or RNA sensing, this work provides an original strategy that can be easily extended to DNA and RNA targets. Nonetheless, the rapid detection of CTCs is crucial because the separation of these tumor cells from primary mass indicates cancer progression. With this aim, rod-like polymer-based microrobots were fabricated by the cryo-cutting of Janus fibers synthesized by electrospinning. The two sides of the microrobots were functionalized with catalase and TLS11a aptamers, respectively: the former provided the self-propulsion ability through the catalyzed H_2O_2 decomposition, and the latter ensured the specific binding of CTCs. Afterward, aptamers were labeled with tetraphenylethylene (TPE) and FITC through base-pair interactions. TPE aggregation-induced emission (AIE) and FITC aggregation-caused quenching (ACQ) effects resulted in blue fluorescence emission. Microrobots movement accelerated the capture of CTCs, inducing the release of TPE and FITC in the solution. Consequently, TPE AIE diminished while FITC green fluorescence was reestablished. This ratiometric fluorescence signaling allowed CTCs detection with a low detection limit of 25 cells mL^{-1} within 1 min exposure to microrobots.

Compared to motion-based detection, fluorescence-based detection is characterized by lower stability over time, for example, due to the fluorophore's photochemical degradation (photobleaching). Additionally, fluorescence microscopy necessitates bulky components, limiting the integration of this method into portable devices.[49]

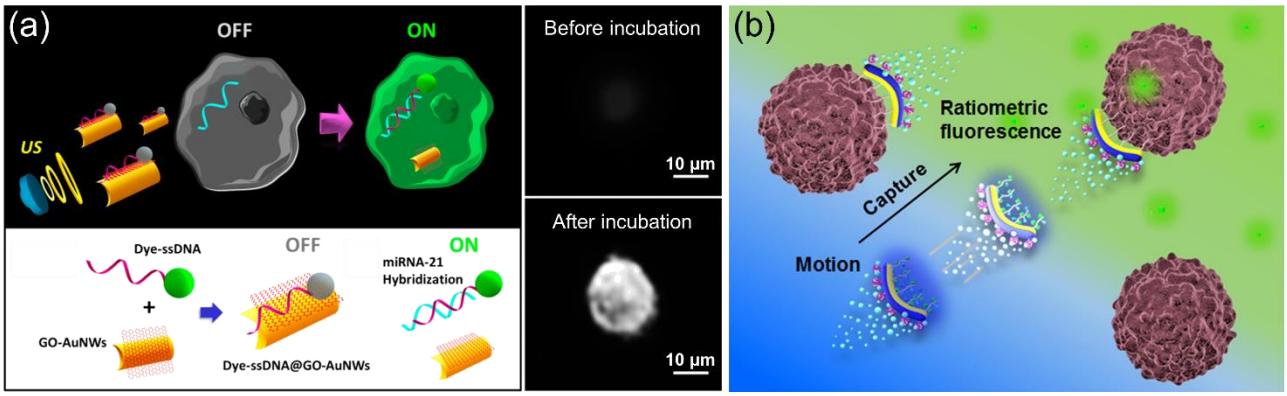

Figure 7. Fluorescence recovery-based sensing strategies. (a) Single-cell miRNA-21 "OFF-ON" fluorescence detection by ultrasound-powered nanorobots; the surface of graphene oxide (GO)/Au nanowires is modified by a dye-labeled ssDNA probe; GO quenches the dye's fluorescence, and the latter is recovered due to the release of the ssDNA probe upon hybridization with the miRNA-21 target. Fluorescence microscopy images of an MCF-7 cell before and after 20 min incubation with nanorobots under an ultrasound field (6 V, 2.66 MHz) demonstrate intracellular miRNA detection. Adapted with permission from [50]. Copyright 2015, American Chemical Society. (b) Ratiometric fluorescence detection of circulating tumor cells (CTCs) by catalase-grafted polymer-based Janus microrobots. The binding between TPE and FITC fluorophores with aptamers on the microrobots' surface resulted in the aggregation-caused quenching (ACQ) effect of FITC and aggregation-induced emission (AIE) of TPE, leading to blue fluorescence emission. CTCs capture caused the release of the fluorophores so that TPE fluorescence was weakened while that of FITC was restored to emit green fluorescence. Reproduced with permission from [53]. Copyright 2020, Elsevier.

4.1.3. Motion- and fluorescence-based detection

Oksuz's research group proposed dual motion- and fluorescence-based detection of miRNA-21 using self-propelled microrobots.[54] Tungsten trioxide (W_5O_{14}) microwires (~100 nm in diameter, ~10 μm in length) were synthesized by chemical vapor transport (CVT) reaction.

PEDOT was polymerized on their surface, followed by the sputtering deposition of a Pt layer. Unlike the previously mentioned approaches, an unlabeled ssDNA probe was immobilized on the microrobots' surface, and a FAM-labeled miRNA-21 target was used. In this way, by exposing the microrobots to 100 nM miRNA-21 in 3% H_2O_2, a remarkable increase in their fluorescence intensity was recorded within 15 min, indicating the successful hybridization between probe and target. At the same time, a notable decline in microrobots' speed was noted, which changed from 420 to 78 μm s^{-1}. This behavior was explained by the complete blocking of the microrobots' surface due to the dsDNA formation. W_5O_{14}/Pt microrobots were tested as a control, showing a lower sensitivity. In fact, PEDOT's larger surface area could accommodate more probe sequences, producing larger fluorescence and speed variations. A linear response was observed over the wide range of 1–100 nM miRNA-21 for both the fluorescence and speed signaling modes, from which low LoD values of 28 pM and 21 pM were calculated, respectively.

The motion and fluorescence-based detection of miRNA-21 was also studied for Au/PEDOT/Pt tubular microrobots (2 μm in diameter, ~12 μm in length) fabricated by membrane template-assisted electrodeposition.[55] In this case, the microrobot surface was modified with a FAM-labeled ssDNA probe through hydrophobic and van der Waals interactions. The fluorescence intensity and speed of the microrobots decreased after 5 min incubation with the miRNA target due to the occurred hybridization. Of note, Au/PEDOT/Pt microrobots' speed (140 μm s^{-1}) was lower than PEDOT/W_5O_{14}/Pt despite the higher amount of H_2O_2 (10%) required for their motion. Additionally, a worse LoD of 0.34 nM was attained. Still, the authors showed microrobots' antiproliferative effect against breast cancer cells.

The application of surface acoustic waves (SAW) was demonstrated to be an effective strategy to lower the miRNA-21 LoD by removing the unbound ssDNA probe from the microrobots' surface.[56] Tubular Au/Pt microrobots (1.5–2 μm in diameter, ~10 μm in length) were prepared by membrane template-assisted electrodeposition and functionalized with a FAM-labeled ssDNA probe. Under the SAW, microrobots' bubble-propulsion speed in 1% H_2O_2 increased from ~30 to 50 μm s^{-1} while the lowered fluorescence intensity confirmed the release of the unbound probe. The beneficial effect of SAW on miRNA-21 response and, thus, LoD were evident as it decreased from 0.41 nM to 0.19 nM for the fluorescence signaling mode.

To avoid using H_2O_2, the same research group proposed miRNA-21 sensing by magnetically and acoustically powered Au–Ni nanorobots.[57] Au nanowires (200 nm in diameter, 3 μm in length) were fabricated by membrane template-assisted electrodeposition

and subsequently coated by a Ni layer through the sputtering technique. This design enabled nanorobots' dual magnetic and acoustic actuation. Nanorobots displayed a speed of 21.5 μm s^{-1} under a constant magnetic field (22 mT, 20 Hz), which further increased to 120 μm s^{-1} by the simultaneous application of an acoustic field (3 dBm). As in the previous examples, the nanorobots' surface was modified with a FAM-labeled ssDNA probe. The hybridization with the miRNA-21 target (0.01–100 nM) significantly quenched nanorobots' fluorescence intensity and speed, resulting in ultra-low detection limit values (2.9 and 1.6 pM, respectively) compared to catalytic microrobots. In addition, the *on-site* delivery of doxorubicin (DOX) to breast cancer cells was also investigated, exploiting the high precision of magnetic actuation.

Independently from the sensing mechanism, all examples presented above were based on the functionalization of the micro/nanorobot's surface with an ssDNA probe for binding a DNA or RNA target. Therefore, their use was limited to the specific target. However, a recent work introduced non-functionalized micro/nanorobots as generic cargo carriers to perform dynamic loading, transport, and release of functionalized beads.[75] In this way, the same micro/nanorobot can be reused for different targets or detect them at the same time as long as adequately functionalized beads are carried.

4.2. Nucleic acids isolation

Nucleic acids isolation is critical for many biomedical and diagnostic applications. However, current methods at the macroscale are unsuitable for microscale devices. Micro/nanorobots' autonomous motion represents a valid solution to this problem. Nucleic acids capture, transport, and delivery by DNA-modified micro/nanorobots rely on the intrinsic specificity of DNA base pairing, allowing to pick up and transport of a selected targeted sequence by immobilizing its complementary sequence on the micro/nanorobot's surface.

Wang's research group demonstrated the rapid extraction of nucleic acids from raw biological samples using DNA-modified self-propelled microrobots.[58] Pt tubular microrobots were prepared by the strain-assisted rolling of functional nanomembranes on polymers,[32] covered with Au by electron beam evaporation and functionalized with an ssDNA probe sequence. A fluorophore-labeled ssDNA target was used. Microrobots' bubble-propulsion in H_2O_2 resulted in a 13-fold enhancement in the hybridization efficiency compared to static ones. This result was attributed to the generation of fluid vortexes that promoted mass transfer. The lower the sample volume, the stronger the local mixing effect produced. The

authors also demonstrated microrobots' movement in untreated complex biological samples (plasma, urine, saliva) to capture the target, which was further transported to a "clean" zone where post-processing analyses (for instance, sensing) could be, in principle, conducted (**Figure 8(a)**).

Besides capture and transport, achieving controlled release of the target is essential for post-treatments. Aptamer-functionalized Au/Ni/Pt tubular microrobots have been employed to reach this goal.[59] Microrobots' surface was modified with a mixed binding aptamer (MBA) containing both thrombin and adenosine triphosphate (ATP) aptamers *via* DNA hybridization. While the first aptamer ensured selective isolation and transport of thrombin, the second allowed the release of the MBA-thrombin complex upon swimming in an ATP solution (**Figure 8(b)**). Such a capture–transport–release approach holds great potential for diverse diagnostic applications.

Similarly, bubble-propelled aptamer-modified Au/Ni/MnO_2-polyethyleneimine (Au/Ni/MnO_2-PEI) nanorobots were used to collect human promyelocytic leukemia cells (HL-60) in human serum.[60] After performing the capture, nanorobots were transferred into a second chamber where HL-60 cells were released in the presence of a nucleotide sequence complementary to the aptamer. Further detection of the released HL-60 cells was carried out using an aptamer-modified electrode by electrochemical impedance spectroscopy (EIS), attaining a low detection limit of 250 cells mL^{-1}.

Surface charge-reversible microrobots enabled the controlled extraction and release of nucleic acids through a different mechanism (**Figure 8(c)**).[61] Tubular microrobots (1–2 μm in diameter, ~10.5 μm in length, ~150 nm in wall thickness), consisting of a ferromagnetic Ni layer embedded in an inner Pt layer and an outer cationic PEI-functionalized PPy-COOH/PPy layer, were prepared by membrane template-assisted electrodeposition and carbodiimide chemistry. This design resulted in high-speed bubble-propelled microrobots (~500 μm s^{-1} in 4% H_2O_2) harboring magnetic properties and pH-dependent surface charge. In acidic solution (pH 4), microrobots' positively charged surface allowed capturing FITC-labeled negatively charged nucleic acids by electrostatic attraction with > 95% efficiency. After being magnetically transferred to a basic solution (pH 11), microrobots' surface turned negative, causing the release of captured nucleic acids with 80% efficiency. Microrobots' excellent reusability and the possibility of guidance in microfluidic channels using an external magnetic field make them particularly attractive for microscale gene isolation. Despite being selective towards proteins, this approach does not allow for selectively picking up and transporting a

specific nucleic acid. In fact, it is based on the electrostatic attraction/repulsion between the microrobots' surface and potential targets in their proximity rather than DNA base pairing.

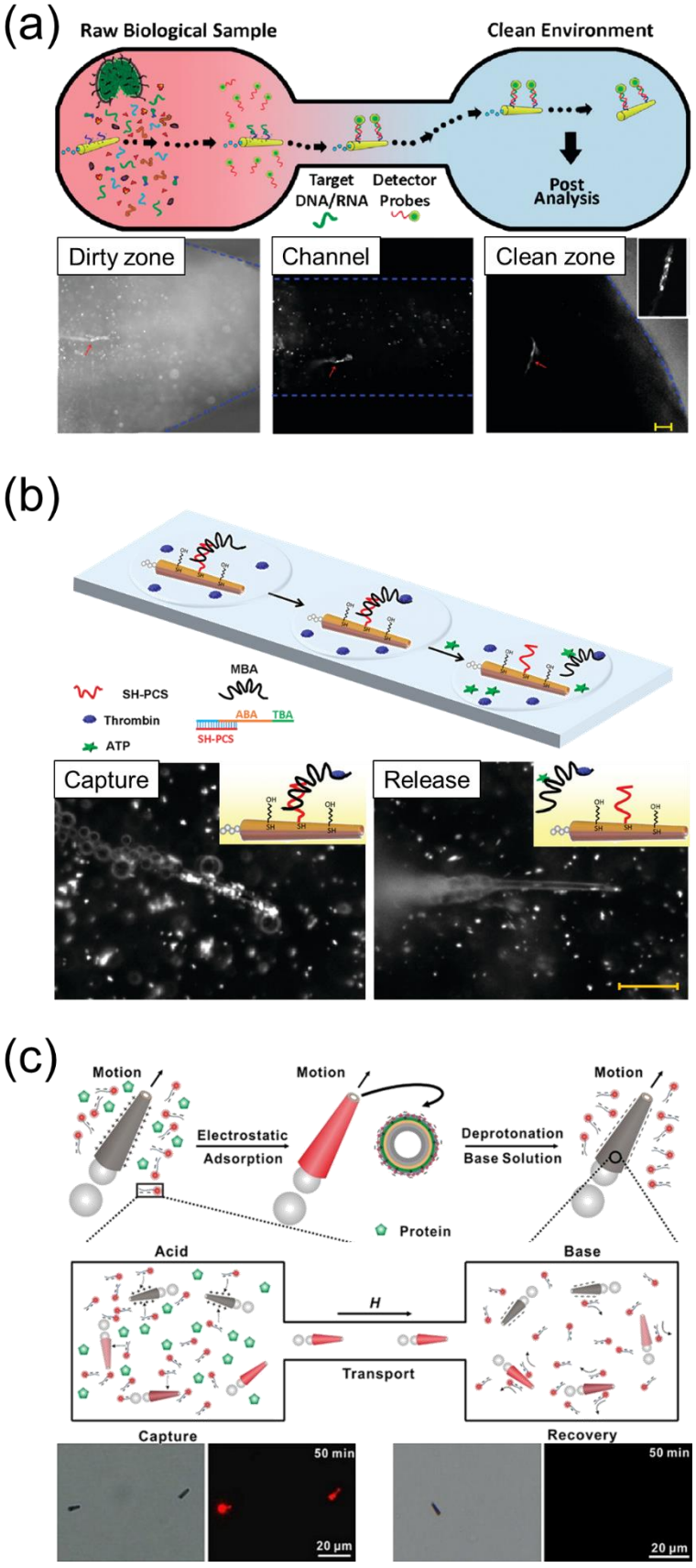

Figure 8. Nucleic acids isolation strategies. (a) Nucleic acids extraction from raw biological samples: optical microscopy images show a bubble-propelled ssDNA probe-modified Au/Pt

tubular microrobot that captures a fluorophore-labeled DNA target *via* hybridization in a "dirty" zone, transports it across a channel, and reaches a "clean" zone for post-analysis. The scale bar is 60 μm (30 μm for the inset). Adapted with permission from [58]. Copyright 2011, American Chemical Society. (b) Isolation and controlled release of proteins: bubble-propelled Ti/Ni/Au/Pt microrobots are modified with a mixed binding aptamer (MBA) containing both thrombin and ATP aptamers; thrombin is captured by its aptamer, transported by microrobots, and released in an ATP solution. Optical microscopy images demonstrate the release of the target protein after 20 min incubation in the absence (left) or presence (right) of 0.01 M ATP. The scale bar is 30 μm. Adapted with permission from [59]. Copyright 2011, American Chemical Society. (c) Nucleic acids extraction by surface charge-reversible microrobots: bubble-propelled magnetic field-navigable PEI-functionalized PPy-COOH/PPy/Ni/Pt tubular microrobots capture FITC-labeled negatively charged nucleic acids in acidic solutions (pH 4) due to their positive surface charge and release them in basic solutions (pH 11) due to their negative surface charge. Optical and fluorescence microscopy images prove nucleic acids' capture by microrobots (50 min in acidic solution) and release (50 min in basic solution). Adapted with permission from [61]. Copyright 2019, Wiley.

4.3. Gene therapy

Gene therapy is a medical treatment based on the delivery of DNA to defective cells to treat or cure a disease or cancer. Lipoplexes, complexes of cationic lipids and anionic DNA linked by ionic interactions, are considered excellent vectors for DNA delivery. They can easily fuse with the cell membrane or be incorporated through endocytosis. Inspired by natural bacteria flagella, lipoplexes-functionalized artificial bacterial flagella have been designed and operated as magnetic microrobots for targeted and single-cell gene therapy (**Figure 9(a)**).[62] Polymeric helical structures (5 μm in diameter, 16 μm in length) were produced by 3D laser direct writing and covered by thin Ni and Ti layers through electron beam evaporation. The Ni core provided the magnetic property required for microrobots navigation based on the mechanism illustrated in Figure 2(e). At the same time, the Ti layer passivated the Ni surface, improving microrobots' biocompatibility and ensuring the facile loading of lipoplexes after oxidation to TiO_2. A rotating magnetic field allowed controlling microrobots' movement toward targeted cells at speed values as high as ~44 μm s^{-1} for a ~30 Hz frequency and 5 mT magnetic field. When employed for *in vitro* HEK 293 cells transfection studies, they showed efficient delivery of the plasmid DNA in the lipoplexes to the cells in their proximity. In fact, the

transfected cells expressed the Venus protein, whose fluorescence has been recorded. Notably, it has been observed that microrobots could transfect cells without influencing cell division or causing cell death, which is fundamental for *in vivo* applications.

Micro/nanorobots are also promising for small interfering RNA (siRNA) therapy. This involves the delivery of gene silencing complexes that suppress mRNA target sequences, inhibiting the expression of unwanted proteins within the cell. A nanorobot-based approach with greatly enhanced intracellular gene delivery and silencing efficiency compared to conventional methods has been demonstrated (**Figure 9(b)**).[63] Au nanowires (200 nm in diameter, ~4 μm in length) were prepared by membrane template-assisted electrodeposition and successively modified with Green Fluorescence Protein-targeted siRNA (siGFP) hybridized to circular DNA structures obtained *via* Rolling Circle Amplification (RCA). The small size and motion of GFP/RCA-Au nanorobots under an ultrasound field (6 V, 2.66 MHz) allowed their rapid internalization inside the cell. Nanorobots' gene silencing ability has been tested in various cell lines, including HEK 293 cells, which were selected as they easily express recombinant proteins like the GFP. Fluorescence signals were recorded after treatments with nanorobots for different incubation times and GFP/RCA loadings with (dynamic) and without (static) applied ultrasound. The fluorescence of samples treated with static nanorobots was almost unchanged compared to the evident decrease observed for dynamic ones, attributed to their spinning movement inside the cells. Cell viability measurements excluded the possibility that GFP silencing was due to cell death caused by nanorobots. In principle, RCA can support multiple siRNA sequences at once, leading to the simultaneous delivery of several siRNA sequences associated with various diseases or cancers.

Acoustically propelled Au nanorobots were employed as well for the intracellular delivery of sgRNA/Cas9 complex, causing GFP knockout in B16F10 cells with an ~80% efficiency for dynamic nanorobots and ~30% for static ones within 2 h incubation.[76]

Despite these preliminary results promising huge prospects, the safety and the fate of these micro/nanorobots inside the body remain to be investigated and demonstrated. Furthermore, for targeted therapy, the micro/nanorobots' imaging is critical and has to be proven not only *in vitro* but also in real-time inside living organisms.

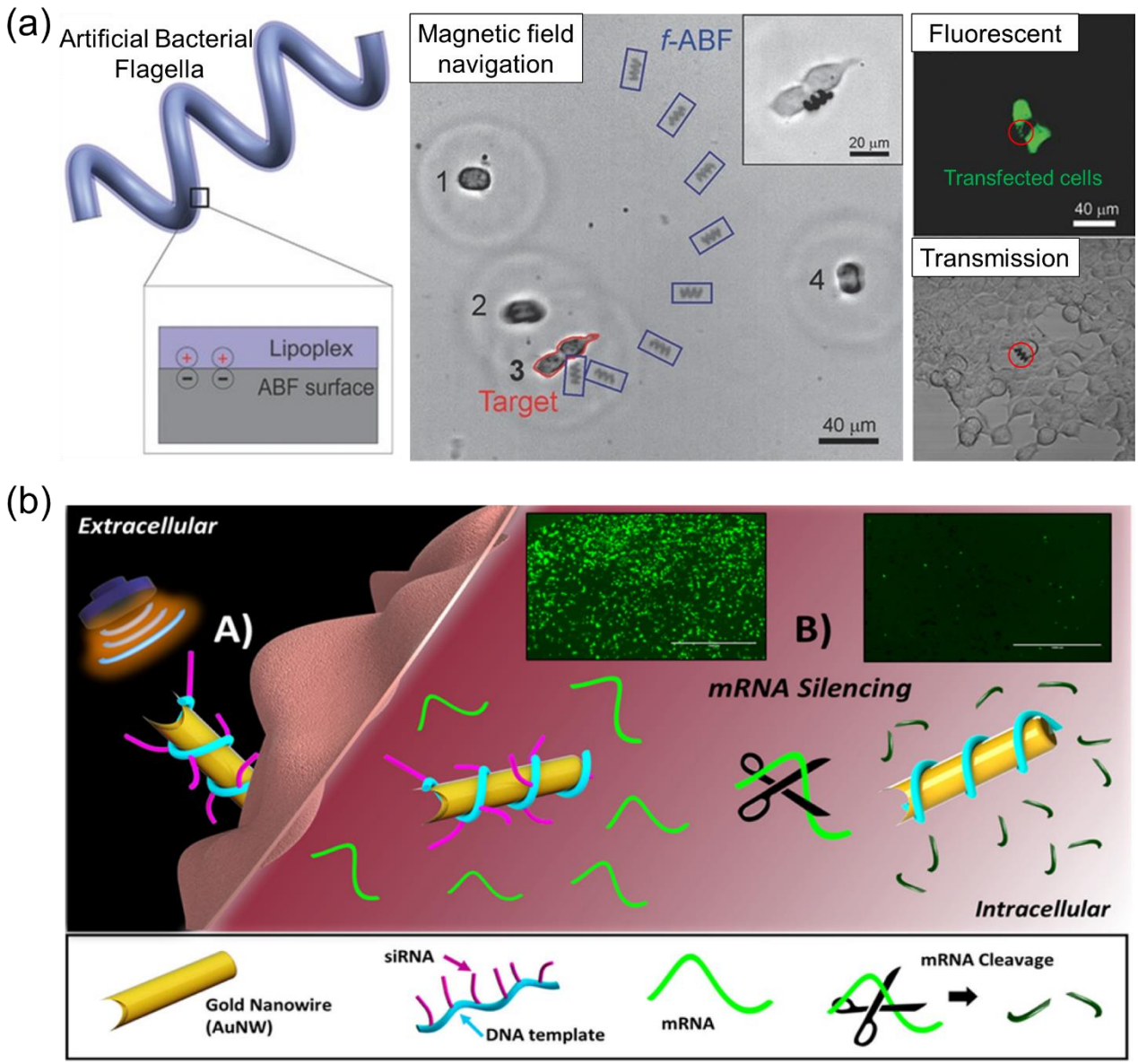

Figure 9. DNA-modified micro/nanorobots for gene therapy. (a) Lipoplexes-functionalized artificial bacteria flagella for targeted gene delivery: time-lapse optical microscopy image shows the precise navigation of a helical microrobot (blue square) toward a targeted HEK 293 cell (undergoing division) under a rotating magnetic field (5 mT, 30 Hz) (the time interval of each microrobot's movement is 4 s). The plasmid DNA in lipoplexes successfully transfects cells. Transmission and fluorescent microscopy images demonstrate encoded protein expression in the transfected cells (red circles indicate the microrobot). Adapted with permission from [62]. Copyright 2015, Wiley. (b) Ultrasound-powered nanorobots for intracellular siRNA delivery: the fast internalization and rapid movement of Au nanowires inside HEK 293-GFP cells accelerate mRNA gene silencing. Fluorescence images demonstrate GFP fluorescence decrease after 5 min treatment with nanorobots under

ultrasound (6 V, 2.66 MHz) and overnight incubation. Scale bars are 1 mm. Reproduced with permission from [63]. Copyright 2016, American Chemical Society.

4.4. Water remediation

The rapid pace of industrialization and diverse human activities have produced various harmful pollutants, including heavy metal ions, nano/microplastics, hazardous chemicals, and pathogens that damage the environment. Mercury is one of the most toxic contaminants in water bodies for wildlife and humans. DNA-functionalized microrobots have been proposed as efficient machines for water purification from mercury.[64] These comprised Au/Pt tubular microrobots prepared by membrane template-assisted electrodeposition (2.5–3 μm in diameter, ~10 μm in length). The Au outer layer ensured a large surface area for immobilizing a thiolated DNA sequence with thymine–thymine (T–T) mismatched base pairs. The mercury sequestration strategy was based on Hg(II) ions' property to selectively mediate the generation of T-Hg(II)-T complexes. In fact, Hg(II) binds to N3 of thymidine by replacing the imino proton and cross-linking two thymidines to form the T-Hg(II)-T base pair. The microrobots showed a high speed of ~180 μm s^{-1} in the presence of 3% H_2O_2. Aqueous solutions containing 3 ppm Hg(II) ions were exposed for 20 min to microrobots in static and dynamic conditions. The solutions were subsequently analyzed by inductively coupled plasma-mass spectrometry (ICP-MS) to evaluate the residual content of Hg(II). The higher removal efficiency was found for the dynamic microrobots (26%) compared to the static ones (17%), attributed to the DNA-induced "on-the-fly" trapping of Hg(II). This result is particularly remarkable considering the low number of microrobots involved in the experiments (~3000 mL^{-1}). Furthermore, the proposed strategy can also be employed for mercury sensing at trace level, which is essential as well as its successive remediation. Nonetheless, given the high concentration of H_2O_2 utilized in these experiments, its residual presence in the treated water samples must be considered. The immobilization of T-T mismatched base pairs onto fuel-free light-powered micro/nanorobots is a valid alternative. Also, the Au/Pt tubular microrobots' design is relatively expensive and may be replaced by cheaper and larger surface area materials.

5. Conclusions and future perspectives

In this review, we presented recent advances in the development and application of DNA-modified micro/nanorobots. First, the most reported mechanisms to power these systems have been introduced, including catalytic, acoustic, and magnetic actuation. Then, new DNA-based propulsion concepts have been illustrated. These comprise the utilization of DNA as a substrate for the chemotactic movement of enzymatic nanorobots toward apoptotic tumor cells, which is promising for drug delivery and, thus, cancer therapy. Nucleospheres, *i.e.*, self-assembled DNA microspheres, are fascinating platforms for the formulation of microrobots due to their easy functionalization through the DNA chemistry. Moreover, the inclusion of DNA nanodevices in the material's design, such as pH-responsive DNA nanoswitches, represents a step forward toward micro/nanorobots' intelligentization, which is one of the biggest challenges in this research field.

The high specificity of DNA base-pairing combined with the motion dimension has opened new possibilities in various applications. For example, the concept of motion-based sensing has been extended to DNA and RNA. Several approaches have been conceived to transduce the probe–target recognition event into a detectable variation of micro/nanorobots' speed, ranging from proof-of-concept reports to compact cellphone-based sensors with a high market value. Most of the studies involved catalytic microrobots fueled by H_2O_2, whose toxicity was not a problem in those specific cases. We also expect the future investigation of magnetic propulsion for motion-based sensing, taking inspiration from the work of Nguyen and Minteer, who presented the "signal-on" DNA detection as a result of the DNA target-induced hybridization between DNA-modified tubular microrobots and Pt nanoparticles.[47] In particular, we propose to replace the Pt nanoparticles with superparamagnetic beads which, once anchored to the microrobot, will unlock its magnetic motion. Then, magnetic actuation could provide more sensitive DNA detection than bubble-propulsion due to more parameters, such as magnetic field intensity and frequency, which can be precisely tuned.

Furthermore, the fast and efficient fluorescence detection of various cancer biomarkers has been proved. The mechanism involved the fluorescence quenching of a dye-labeled ssDNA probe on the micro/nanorobots' surface, followed by the fluorescence recovery due to its hybridization with the target. In addition, dual motion and fluorescent-based signaling has been reported. In these works, acoustically powered micro/nanorobots have been preferred, especially when the detection was performed in living cells. Specifically, ultrasound-powered nanorobots showed rapid internalization and effective movement inside the cell.

Different approaches for the "on-the-fly" capture, transport, and release of nucleic acids have been proposed, playing on DNA hybridization, DNA aptamer-protein binding, and

microrobots' reversible surface charge. These pose the basis for developing an all-in-one microfluidic device for targeted DNA isolation from a chamber where the raw sample is introduced to a clean chamber for post-processing analyses, such as sensing. Such a device would truly represent an important advance compared to conventional methods for DNA detection, avoiding complex and multiple sample preparation and washing steps. For this purpose, the micro/nanorobot's design must comprise at least one or two components for the propulsion (for example, a catalytic engine to accelerate the recognition and a magnetic element for the controlled manipulation throughout the device), a recognition unit, and a sensing unit. Nevertheless, the fabrication of multi-task micro/nanorobots is challenging.[28]

DNA-modified micro/nanorobots have great potential in precision medicine, allowing intracellular gene delivery to promote or suppress the expression of specific proteins. However, several challenges have to be overcome for their clinical translation.[77] The first one is related to their safety, which must be demonstrated following the stringent rules of the most accreditated regulations agencies. Micro/nanorobots' toxicity and immune response studies must be conducted through animal testing, considering that these results do not always translate to humans. After completing their tasks, they must be expelled from the body or reabsorbed without posing any risk. In this regard, biocompatible and biodegradable materials have to be taken into account in the micro/nanorobots' design. The control over the position and the real-time imaging of micro/nanorobots are the other two key factors. Acoustic actuation and magnetic actuation allow safe operation, being the ideal candidates for medical applications. Notably, magnetic micro/nanorobots can be accurately navigated toward the targeted cell. It is worth noting that both classes of micro/nanomachines usually enter the cells by physical penetration, which can cause the cell's death. Hence, less invasive internalization strategies should also be explored. Finally, the advantages in terms of higher efficiency and lower costs and risks compared to the conventional therapeutic approaches must be proven to transform these proof-of-concept studies into commercial products. In this context, 3D bioprinting will play a crucial role in the large-scale and low-cost manufacturing of medical micro/nanorobots.

The original utilization of mismatched DNA-modified microrobots for selectively removing Hg(II) from Hg-polluted waters has also been proven.

As the fields of DNA nanotechnology and micro/nanorobotics are progressing rapidly, we believe that novel, exciting directions will emerge soon. In this regard, inspired by the movie "Big Hero 6" showing tiny microbots linking together in any arrangement thanks to a neurocranial transmitter, we foresee the formulation of complex, intelligent, and

programmable nanorobotic swarms taking advantage of the high programmability of DNA interactions. Although total control over the assembly has not been achieved yet, the foundations have already been laid: DNA-coated colloids have been used to design sophisticated materials at the colloidal scale with tailored surfaces, shapes, and structures.[78] Two particles (blue and red) were modified with complementary A and B DNA strands, respectively, and self-complementary P DNA strands (**Figure 10(a)**). The displacement strands D_A and D_B, complementary to A and B strands, consented to control the activation of the A and B strands' sticky ends with the temperature. Below the melting temperature of the P-P binding (<35°C), particles could self-assemble only with particles of the same color through P-P hybridization since the displacements strands deactivated the A and B strands (**Figure 10(b)**). At temperatures ranging between 36 and 44°C, the P-P bindings were broken, and the particles were separated. Above 45°C, the A-D_A and B-D_B bindings were molten, allowing the association between blue and red particles. Finally, above 65°C, the A and B strands dehybridized, and the particles were dispersed again. Varying the size ratio and increasing the number of particles allows the formulation of a limitless number and type of structures depending on the temperature. For instance, blue and red particles (1:0.6 size ratio) could form fcc structures of different sizes at a lower temperature which assembled into a single AlB_2 structure at a higher temperature (**Figure 10(c)**). On the other hand, the ternary system composed of blue, red, and self-complementary yellow particles (1:1:0.6 size ratio) resulted in two different structures at a lower temperature (CsCl structure made of blue and red particles, and an fcc structure constituted by yellow particles), which recrystallized into a single AlB_2 structure at a higher temperature.[79] The possibility of introducing external stimuli, such as the temperature or light, to trigger or influence the assembly/disassembly of self-motile micro/nanorobots further expands their potential. Indeed, DNA-engineered nanorobots can, in principle, possess the encoding information for their self-assembly into self-propelled superstructures performing tasks beyond a single entity's capability.

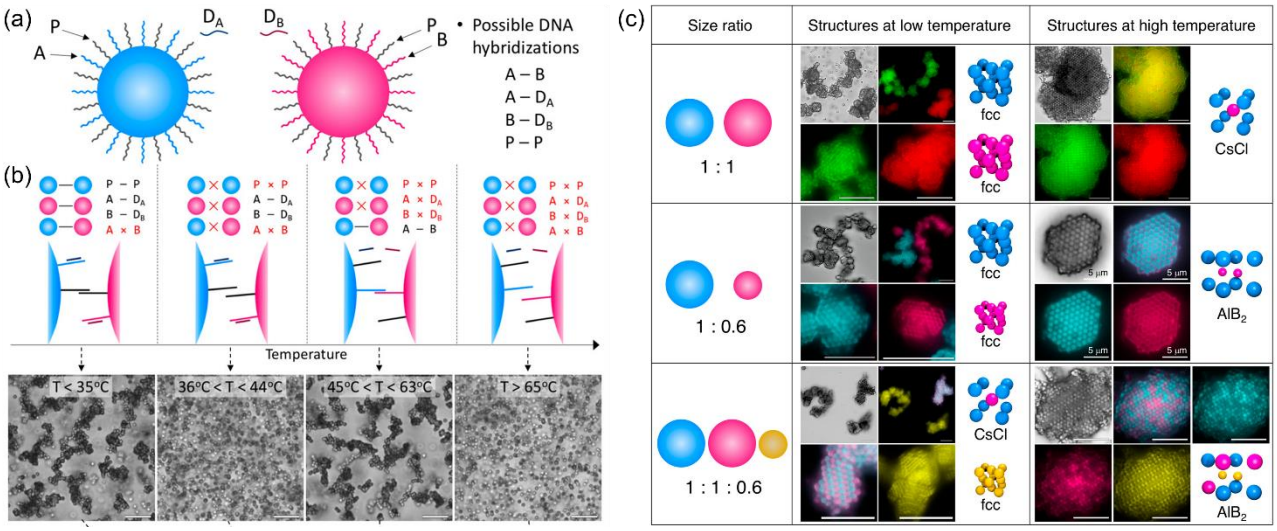

Figure 10. Reconfigurable self-assembly of DNA-coated particles in response to temperature. (a) Schematic illustration of the reconfigurable self-assembly of two DNA-coated particles of the same size at different temperatures. The blue and red particles are coated with A and B complementary strands, respectively, and self-complementary P DNA strands. D_A and D_B are displacement strands for A and B DNA strands, respectively, allowing to control their activation/deactivation. (b) Schematic illustration of the specific interactions between DNA-coated particles and the available DNA−DNA bonds, and the corresponding optical images of the DNA-coated particles at different temperatures. (c) DNA-coated particles of various size ratios are programmed to self-assemble into separate crystals at the lower temperature and a single, different crystal at the higher temperature. Scale bars are 10 μm. Adapted with permission from [79]. Copyright 2020, American Chemical Society.

Acknowledgments

M.P. was supported by the Ministry of Education, Youth and Sports (Czech Republic) grant LL2002 under the ERC CZ program. M.U. acknowledges financial support by the European Union's Horizon 2020 research and innovation program under the Marie Skłodowska-Curie grant agreement No. 101038066.

Received: ((will be filled in by the editorial staff))
Revised: ((will be filled in by the editorial staff))
Published online: ((will be filled in by the editorial staff))

References

[1] C. H. Lu, B. Willner, I. Willner, *ACS Nano* **2013**, *7*, 8320.

[2] N. C. Seeman, *Nature* **2003**, *421*, 427.

[3] Y. J. Chen, B. Groves, R. A. Muscat, G. Seelig, *Nat. Nanotechnol.* **2015**, *10*, 748.

[4] N. C. Seeman, H. F. Sleiman, *Nat. Rev. Mater.* **2018**, *3*, 17068.

[5] M. Madsen, K. V. Gothelf, *Chem. Rev.* **2019**, *119*, 6384.

[6] Y. Zhao, X. Dai, F. Wang, X. Zhang, C. Fan, X. Liu, *Nano Today* **2019**, *26*, 123.

[7] Q. Hu, H. Li, L. Wang, H. Gu, C. Fan, *Chem. Rev.* **2019**, *119*, 6459.

[8] L. Shen, P. Wang, Y. Ke, *Adv. Healthc. Mater.* **2021**, *10*, 2002205.

[9] F. Soto, E. Karshalev, F. Zhang, B. Esteban Fernandez De Avila, A. Nourhani, J. Wang, *Chem. Rev.* **2021**, *122*, 5365.

[10] F. Novotný, H. Wang, M. Pumera, *Chem* **2020**, *6*, 867.

[11] M. Ussia, M. Pumera, *Chem. Soc. Rev.* **2022**, *51*, 1558.

[12] B. Wang, K. Kostarelos, B. J. Nelson, L. Zhang, *Adv. Mater.* **2021**, *33*, 2002047.

[13] S. Yu, Y. Cai, Z. Wu, Q. He, *View* **2021**, *2*, 20200113.

[14] K. Xu, B. Liu, *Beilstein J. Nanotechnol.* **2021**, *12*, 756.

[15] C. K. Schmidt, M. Medina-Sánchez, R. J. Edmondson, O. G. Schmidt, *Nat. Commun.* **2020**, *11*, 5618.

[16] H. Ye, Y. Wang, D. Xu, X. Liu, S. Liu, X. Ma, *Appl. Mater. Today* **2021**, *23*, 101007.

[17] Z. Wu, Y. Chen, D. Mukasa, O. S. Pak, W. Gao, *Chem. Soc. Rev.* **2020**, *49*, 8088.

[18] Y. Hu, W. Liu, Y. Sun, *Adv. Funct. Mater.* **2021**, 2109181.

[19] M. Urso, M. Pumera, *Adv. Funct. Mater.* **2022**, 2112120.

[20] C. M. Oral, M. Ussia, M. Pumera, *J. Phys. Chem. C* **2021**, *125*, 18040.

[21] X. Peng, H. Zhu, H. Chen, X. Feng, R. Liu, Z. Huang, Q. Shen, Y. Ma, L. Wang, *New J. Chem.* **2019**, *43*, 12594.

[22] A. Bazrafshan, M. E. Kyriazi, B. A. Holt, W. Deng, S. Piranej, H. Su, Y. Hu, A. H. El-Sagheer, T. Brown, G. A. Kwong, A. G. Kanaras, K. Salaita, *ACS Nano* **2021**, *15*, 8427.

[23] H. Ramezani, H. Dietz, *Nat. Rev. Genet.* **2020**, *21*, 5.

[24] M. Urso, M. Ussia, M. Pumera, *Adv. Funct. Mater.* **2021**, *31*, 2101510.

[25] M. Ussia, M. Urso, K. Dolezelikova, H. Michalkova, V. Adam, M. Pumera, *Adv. Funct. Mater.* **2021**, *31*, 2101178.

[26] X. Peng, M. Urso, M. Pumera, *Small Methods* **2021**, *5*, 2100617.

[27] C. M. Oral, M. Ussia, D. K. Yavuz, M. Pumera, *Small* **2022**, *18*, 2106271.

[28] J. Wang, *Nat. Commun.* **2021**, *12*, 7125.

[29] L. Wang, Z. Meng, Y. Chen, Y. Zheng, *Adv. Intell. Syst.* **2021**, *3*, 2000267.

[30] M. Urso, C. Iffelsberger, C. C. Mayorga-Martinez, M. Pumera, *Small Methods* **2021**, *5*, 2100511.

[31] J. Muñoz, M. Urso, M. Pumera, *Angew. Chemie - Int. Ed.* **2022**, *61*, e202116090.

[32] A. A. Solovev, Y. Mei, E. B. Ureña, G. Huang, O. G. Schmidt, *Small* **2009**, *5*, 1688.

[33] J. Li, I. Rozen, J. Wang, *ACS Nano* **2016**, *10*, 5619.

[34] W. F. Paxton, P. T. Baker, T. R. Kline, Y. Wang, T. E. Mallouk, A. Sen, *J. Am. Chem. Soc.* **2006**, *128*, 14881.

[35] J. Wang, W. Gao, *ACS Nano* **2012**, *6*, 5745.

[36] S. Hermanová, M. Pumera, *Chem. - A Eur. J.* **2020**, *26*, 11085.

[37] H. Yuan, X. Liu, L. Wang, X. Ma, *Bioact. Mater.* **2021**, *6*, 1727.

[38] A. C. Hortelao, C. Simó, M. Guix, S. Guallar-Garrido, E. Julián, D. Vilela, L. Rejc, P. Ramos-Cabrer, U. Cossío, V. Gómez-Vallejo, T. Patiño, J. Llop, S. Sánchez, *Sci. Robot.* **2021**, *6*, eabd2823.

[39] P. L. Venugopalan, B. Esteban-Fernández De Ávila, M. Pal, A. Ghosh, J. Wang, *ACS Nano* **2020**, *14*, 9423.

[40] L. Xu, D. Gong, K. Chen, J. Cai, W. Zhang, *J. Appl. Phys.* **2020**, *128*, 184703.

[41] M. Fernández-Medina, M. A. Ramos-Docampo, O. Hovorka, V. Salgueiriño, B. Städler, *Adv. Funct. Mater.* **2020**, *30*, 1908283.

[42] Y. Ye, F. Tong, S. Wang, J. Jiang, J. Gao, L. Liu, K. Liu, F. Wang, Z. Wang, J. Ou, B. Chen, D. A. Wilson, Y. Tu, F. Peng, *Nano Lett.* **2021**, *21*, 8086.

[43] H. Inaba, K. Hatta, K. Matsuura, *ACS Appl. Bio Mater.* **2021**, *4*, 5425.

[44] T. Patino, A. Porchetta, A. Jannasch, A. Lladó, T. Stumpp, E. Schäffer, F. Ricci, S. Sánchez, *Nano Lett.* **2019**, *19*, 3440.

[45] M. Hoop, F. Mushtaq, C. Hurter, X. Z. Chen, B. J. Nelson, S. Pané, *Nanoscale* **2016**, *8*, 12723.

[46] J. Wu, S. Balasubramanian, D. Kagan, K. M. Manesh, S. Campuzano, J. Wang, *Nat. Commun.* **2010**, *1*, 36.

[47] K. Van Nguyen, S. D. Minteer, *Chem. Commun.* **2015**, *51*, 4782.

[48] X. Zhang, C. Chen, J. Wu, H. Ju, *ACS Appl. Mater. Interfaces* **2019**, *11*, 13581.

[49] M. S. Draz, K. M. Kochehbyoki, A. Vasan, D. Battalapalli, A. Sreeram, M. K. Kanakasabapathy, S. Kallakuri, A. Tsibris, D. R. Kuritzkes, H. Shafiee, *Nat. Commun.* **2018**, *9*, 4282.

[50] B. Esteban-Fernández De Ávila, A. Martín, F. Soto, M. A. Lopez-Ramirez, S. Campuzano, G. M. Vásquez-Machado, W. Gao, L. Zhang, J. Wang, *ACS Nano* **2015**,

9, 6756.

[51] D. F. Báez, G. Ramos, A. Corvalán, M. L. Cordero, S. Bollo, M. J. Kogan, *Sensors Actuators, B Chem.* **2020**, *310*, 127843.

[52] V. V. Singh, K. Kaufmann, B. E. F. de Ávila, E. Karshalev, J. Wang, *Adv. Funct. Mater.* **2016**, *26*, 6270.

[53] L. Zhao, Y. Liu, S. Xie, P. Ran, J. Wei, Q. Liu, X. Li, *Chem. Eng. J.* **2020**, *382*, 123041.

[54] G. C. Cogal, G. Y. Karaca, E. Uygun, F. Kuralay, L. Oksuz, M. Remskar, A. U. Oksuz, *Anal. Chim. Acta* **2020**, *1138*, 69.

[55] G. Yurdabak Karaca, F. Kuralay, O. Bingol Ozakpinar, E. Uygun, U. Koc, S. Ulusoy, G. Bosgelmez Tinaz, L. Oksuz, A. Uygun Oksuz, *Appl. Nanosci.* **2021**.

[56] G. Celik Cogal, P. K. Das, G. Yurdabak Karaca, V. R. Bhethanabotla, A. Uygun Oksuz, *ACS Appl. Bio Mater.* **2021**, *4*, 7932.

[57] G. Y. Karaca, F. Kuralay, E. Uygun, K. Ozaltin, S. E. Demirbuken, B. Garipcan, L. Oksuz, A. U. Oksuz, *ACS Appl. Nano Mater.* **2021**, *4*, 3377.

[58] D. Kagan, S. Campuzano, S. Balasubramanian, F. Kuralay, G. U. Flechsig, J. Wang, *Nano Lett.* **2011**, *11*, 2083.

[59] J. Orozco, S. Campuzano, D. Kagan, M. Zhou, W. Gao, J. Wang, *Anal. Chem.* **2011**, *83*, 7962.

[60] M. Amouzadeh Tabrizi, M. Shamsipur, R. Saber, S. Sarkar, *Biosens. Bioelectron.* **2018**, *110*, 141.

[61] M. Luo, Y. Jiang, J. Su, Z. Deng, F. Mou, L. Xu, J. Guan, *Chem. - An Asian J.* **2019**, *14*, 2503.

[62] F. Qiu, S. Fujita, R. Mhanna, L. Zhang, B. R. Simona, B. J. Nelson, *Adv. Funct. Mater.* **2015**, *25*, 1666.

[63] B. Esteban-Fernández De Ávila, C. Angell, F. Soto, M. A. Lopez-Ramirez, D. F. Báez, S. Xie, J. Wang, Y. Chen, *ACS Nano* **2016**, *10*, 4997.

[64] H. Wang, B. Khezri, M. Pumera, *Chem* **2016**, *1*, 473.

[65] A. M. Maier, C. Weig, P. Oswald, E. Frey, P. Fischer, T. Liedl, *Nano Lett.* **2016**, *16*, 906.

[66] M. Urso, S. Tumino, E. Bruno, S. Bordonaro, D. Marletta, G. R. Loria, A. Avni, Y. Shacham-Diamand, F. Priolo, S. Mirabella, *ACS Appl. Mater. Interfaces* **2020**, *12*, 50143.

[67] D. Kagan, P. Calvo-Marzal, S. Balasubramanian, S. Sattayasamitsathit, K. M. Manesh,

G. U. Flechsig, J. Wang, *J. Am. Chem. Soc.* **2009**, *131*, 12082.

[68] Y. Xie, S. Fu, J. Wu, J. Lei, H. Ju, *Biosens. Bioelectron.* **2017**, *87*, 31.

[69] S. Fu, X. Zhang, Y. Xie, J. Wu, H. Ju, *Nanoscale* **2017**, *9*, 9026.

[70] Y. Fang, L. Zhang, Z. Li, Y. Li, C. Huang, X. Lu, *MicroRNAs in DNA Damage Response, Carcinogenesis, and Chemoresistance*, 1st ed., Vol. 333, Elsevier Inc., **2017**.

[71] J. R. Qualliotine, G. Bolat, M. Beltrán-Gastélum, B. E. F. de Ávila, J. Wang, J. A. Califano, *Otolaryngol. - Head Neck Surg.* **2019**, *161*, 814.

[72] M. Beltrán-Gastélum, B. Esteban-Fernández de Ávila, H. Gong, P. L. Venugopalan, T. Hianik, J. Wang, V. Subjakova, *ChemPhysChem* **2019**, *20*, 3177.

[73] B. Esteban-Fernández De Ávila, M. A. Lopez-Ramirez, D. F. Báez, A. Jodra, V. V. Singh, K. Kaufmann, J. Wang, *ACS Sensors* **2016**, *1*, 217.

[74] Á. Molinero-Fernández, M. Moreno-Guzmán, M. Á. López, A. Escarpa, *Anal. Chem.* **2017**, *89*, 10850.

[75] S. Park, G. Yossifon, *ACS sensors* **2020**, *5*, 936.

[76] M. Hansen-Bruhn, B. E. F. de Ávila, M. Beltrán-Gastélum, J. Zhao, D. E. Ramírez-Herrera, P. Angsantikul, K. Vesterager Gothelf, L. Zhang, J. Wang, *Angew. Chemie - Int. Ed.* **2018**, *57*, 2657.

[77] F. Soto, J. Wang, R. Ahmed, U. Demirci, *Adv. Sci.* **2020**, *7*, 2002203.

[78] W. B. Rogers, W. M. Shih, V. N. Manoharan, *Nat. Rev. Mater.* **2016**, *1*, 16008.

[79] J. S. Oh, G. R. Yi, D. J. Pine, *ACS Nano* **2020**, *14*, 4595.

Mario Urso is a Marie Skłodowska-Curie Fellow in the Future Energy & Innovation Lab at the Central European Institute of Technology (CEITEC), Brno, Czech Republic. He received his Ph.D. in Materials Science and Nanotechnology in 2020 from the University of Catania, Italy. Currently, his main scientific interests include the development of self-propelled micro- and nanorobots for environmental remediation, sensing, and electrochemistry.

Martin Pumera is the Director of the Center for Advanced Functional Nanorobots and a Distinguished Professor of Chemistry at the University of Chemistry and Technology, Prague, and Chief Investigator of Future Energy & Innovation Lab at CEITEC, Brno, Czech Republic. He received his Ph.D. in 2001 from Charles University, Czech Republic. He became a tenured group leader at National Institute for Materials Science (NIMS), Japan, in 2006 and joined Nanyang Technological University, Singapore, as a tenured associate professor in 2010. He has interests in nanomaterials, 3D printing, electrochemistry, and micro/nanomachines. He is “Highly Cited Researcher” by Clarivate Analytics since 2017.

The functionalization of self-propelled micro- and nanostructures is the key to developing intelligent and versatile micro/nanorobots. The high specificity and programmability of Watson–Crick base pairing make DNA an ideal functional component for micro/nanorobots. This review discusses the designs, motion mechanisms, and applications of DNA-modified micro/nanorobots, including a perspective on future directions in the field.

M. Urso, M. Pumera*

Micro- and Nanorobots meet DNA